

NASA/CR-20220002035



Development and Application of Advanced Measurement Techniques for Characterizing and Controlling Flow Instabilities in Axial Turbomachines

Joseph Katz
Johns Hopkins University, Baltimore, Maryland

September 2022

NASA STI Program . . . in Profile

Since its founding, NASA has been dedicated to the advancement of aeronautics and space science. The NASA Scientific and Technical Information (STI) Program plays a key part in helping NASA maintain this important role.

The NASA STI Program operates under the auspices of the Agency Chief Information Officer. It collects, organizes, provides for archiving, and disseminates NASA's STI. The NASA STI Program provides access to the NASA Technical Report Server—Registered (NTRS Reg) and NASA Technical Report Server—Public (NTRS) thus providing one of the largest collections of aeronautical and space science STI in the world. Results are published in both non-NASA channels and by NASA in the NASA STI Report Series, which includes the following report types:

- TECHNICAL PUBLICATION. Reports of completed research or a major significant phase of research that present the results of NASA programs and include extensive data or theoretical analysis. Includes compilations of significant scientific and technical data and information deemed to be of continuing reference value. NASA counter-part of peer-reviewed formal professional papers, but has less stringent limitations on manuscript length and extent of graphic presentations.
- TECHNICAL MEMORANDUM. Scientific and technical findings that are preliminary or of specialized interest, e.g., “quick-release” reports, working papers, and bibliographies that contain minimal annotation. Does not contain extensive analysis.
- CONTRACTOR REPORT. Scientific and technical findings by NASA-sponsored contractors and grantees.
- CONFERENCE PUBLICATION. Collected papers from scientific and technical conferences, symposia, seminars, or other meetings sponsored or co-sponsored by NASA.
- SPECIAL PUBLICATION. Scientific, technical, or historical information from NASA programs, projects, and missions, often concerned with subjects having substantial public interest.
- TECHNICAL TRANSLATION. English-language translations of foreign scientific and technical material pertinent to NASA's mission.

For more information about the NASA STI program, see the following:

- Access the NASA STI program home page at <http://www.sti.nasa.gov>
- E-mail your question to help@sti.nasa.gov
- Fax your question to the NASA STI Information Desk at 757-864-6500
- Telephone the NASA STI Information Desk at 757-864-9658
- Write to:
NASA STI Program
Mail Stop 148
NASA Langley Research Center
Hampton, VA 23681-2199

NASA/CR-20220002035



Development and Application of Advanced Measurement Techniques for Characterizing and Controlling Flow Instabilities in Axial Turbomachines

*Joseph Katz
Johns Hopkins University, Baltimore, Maryland*

Prepared under Grant NNX17AH42A

National Aeronautics and
Space Administration

Glenn Research Center
Cleveland, Ohio 44135

September 2022

Trade names and trademarks are used in this report for identification only. Their usage does not constitute an official endorsement, either expressed or implied, by the National Aeronautics and Space Administration.

Level of Review: This material has been technically reviewed by expert reviewer(s).

Development and Application of Advanced Measurement Techniques for Characterizing and Controlling Flow Instabilities in Axial Turbomachines

Joseph Katz
Johns Hopkins University
Baltimore, Maryland 21218

Summary and Report Outline

This report summarizes the recent progress in a project aimed at characterizing the flow structure, instabilities, and turbulence in axial compressors, and also on the utilization of casing grooves for delaying the onset of stall without performance degradation at high flow rates. Progress had been hindered by the COVID-19 laboratory closures and restrictions on the number of people that could be present in the laboratory during Fiscal Year 2020. Once the restrictions were lifted, the tasks described in this report were completed.

The experiments were performed in a refractive-index-matched one-and-half-stage axial compressor and consisted mostly of stereo particle image velocimetry (SPIV) measurements. Whereas prior research focused on detailed measurements of tip flows, with and without casing grooves, the recent campaign had been extended to the entire passage. To enhance the understanding of how the grooves modify the passage flows, measurements were performed in a series of axial (r, θ) planes, extending from the tip to the hub of the machine, covering an entire passage. The mean velocity (all three components) and turbulence measurements were performed upstream of the inlet guide vane (IGV), the IGV-rotor gap, the rotor-stator gap, and downstream of the stator, both without and with semicircular axial casing grooves located around the rotor leading edge. Additional measurements aimed at elucidating mechanisms were performed in axial planes dissecting the rotor and stator passages. Data were acquired at two flow rates, the first corresponding to pre-stall conditions and the second to the best efficiency point (BEP) of the untreated endwall. For each flow rate, the measurements were performed at several rotor orientations.

The data demonstrate that the grooves modify the flow structure over the entire passage, not only in the tip region. Without grooves and under pre-stall conditions, there is a substantial axial blockage and an increase in circumferential velocity in the tip region along with a corresponding increase in axial velocity in the hub area. This blockage is directly associated with tip leakage flow structures, including the leakage flow, the near-circumferential alignment of the tip leakage vortex (TLV), and the intermittent backflow vortices (BFVs). The low-momentum region extends to nearly half of the span at the exit from the rotor. Specific flow mechanisms involved are elucidated. The turbulence is particularly high at the transition between these regions. Once added, the semicircular grooves entrain parts of the TLV, inhibit formation of BFV, and cause periodic variations in flow angle at the blade leading edge (LE). Also, secondary flows generated by the outflow from the grooves at their upstream end bring high axial momentum fluid from the midpassage to the tip region, making the velocity distribution more homogeneous and reducing the turbulence level. The flow inhomogeneity diminishes, and the turbulence level decreases rapidly in the stator passage. The only exception is the suction side (SS) boundary layer of the stator blade, where the flow separates intermittently, increases the turbulence there, and thickens the blade wake. With the grooves, the velocity distribution becomes further homogenized, and the blade wake signature becomes thinner. At the BEP, the effect of the grooves on the distribution of momentum is more subtle, but they expand the area with elevated turbulence in the tip region, consistent with previous observations in meridional planes. Within the stator passage, the ensemble-averaged flow fields with and without the grooves are quite similar. Further trends are examined based on analysis of the passage-averaged velocity profiles. For example, at

pre-stall, although the grooves affect the axial velocity over the entire blade span, the circumferential velocity component is only affected near the casing. In contrast, at the BEP the grooves reduce the circumferential velocity throughout the blade span.

Preliminary results of the measurements described in this report have been presented in the 2021 ASME Turbo Expo (Ref. 1), and a comprehensive pair of publications has been submitted for the 2022 conference (Refs. 2 and 3). Two additional papers focusing on earlier data about tip flows and turbulence have been published in the Journal of Turbomachinery in 2021 (Refs. 4 and 5). Another paper focusing on the structure of turbulence in the tip region has been presented in the 2021 Turbo Expo, and accepted for publication in the Journal of Turbomachinery, scheduled for early 2022 (Ref. 6). The experimental setup, location of measurements, and a table summarizing all the data recorded under this project are presented in Section 2.0. The results are presented in Section 3.0. The mean flow for pre-stall flow rate is presented in Section 2.1, and for the BEP in Section 2.2. Passage-averaged profiles are discussed in Section 2.3. The structure and mechanisms affecting the evolution of turbulence in the passage at pre-stall are discussed in Section 2.4, and those close to the BEP, in Section 3.5. Concluding remarks are provided in Section 3.0.

1.0 Experimental Setup and Summary of Recorded Data

The experiments were performed in the refractive-index-matched facility at Johns Hopkins University, which has been described in prior publications (Refs. 1, 4, and 6 to 21). The blades (Figure 1(a)) are based on the Low Speed Axial Compressor (LSAC) facility at the NASA Glenn Research Center (Refs. 22 and 23). All the measurements were performed with the machine operating at 480 rpm, resulting in a Reynolds number of 1.07×10^6 , based on a tip speed and rotor chord length. The location of axial planes, where the measurements have been performed for a smooth endwall are illustrated in Figure 1(a) and listed in Table I. The measurements with the semicircular axial casing grooves (ACGs) included were only performed between blade rows; that is, the planes identified as pre-IGV, pre-rotor, post-rotor, and post-stator planes. Measurements intersecting with the blades were not able to be made at this time, as initially hoped. The location of the pre-rotor plane relative to the semicircular ACGs is presented in Figure 1(b). Some of the groove dimensions are shown on the figure; additional details can be found in Chen et al. (Refs. 7 and 21), and prior numerical studies involving these grooves are described in Muller et al. (Ref. 24). As is evident, the pre-rotor plane dissects the outlet (upstream) end of the grooves, facilitating measurements of groove-passage flow interactions.

The velocity measurements have been performed using SPIV. The optical setup is illustrated in Figure 2, and technical details about calibration, uncertainty, resolution, and so forth, have been described in prior publications and reports. The axial planes have been illuminated by a 1-mm-thick Nd:YAG laser sheet, and images have been recorded by a pair of 6600×4400 pixel interline transfer charge-coupled device (CCD) cameras. The present fields of view cover the entire span of the machine and extend circumferentially to more than one rotor (or stator) passage. The vector spacing is 0.54 mm for the pre-rotor plane, 0.61 mm for the post-rotor plane, and 0.63 mm for the post-stator plane. In the planes dissecting the rotor, the spacing is 0.60 to 0.62 mm. Data have been acquired for four different rotor orientations, defined based on the circumferential angle Θ between the rotor tip leading edge and the vertical direction. These blade tip orientations are $\Theta = 0^\circ, 12^\circ, 24^\circ, \text{ and } 36^\circ$, enabling the observation of how the relative angle between the rotor and IGV affect the flow structure and turbulence. In the following discussions, the instantaneous radial, circumferential, and axial velocity components are denoted as $u_r, u_\theta, \text{ and } u_z$, respectively. The corresponding ensemble-averaged velocity components for a specific blade orientation are $U_r, U_\theta, \text{ and } U_z$; the velocity fluctuations are $u'_i = u_i - U_i$; and ensemble-averaged Reynolds stress components are $\langle u'_i u'_j \rangle$. The turbulent kinetic energy (TKE) is $k = 0.5(\langle u'_r u'_r \rangle + \langle u'_\theta u'_\theta \rangle + \langle u'_z u'_z \rangle)$. The instantaneous and ensemble-averaged vorticity components are ω_i and $\langle \omega_i \rangle$, respectively.

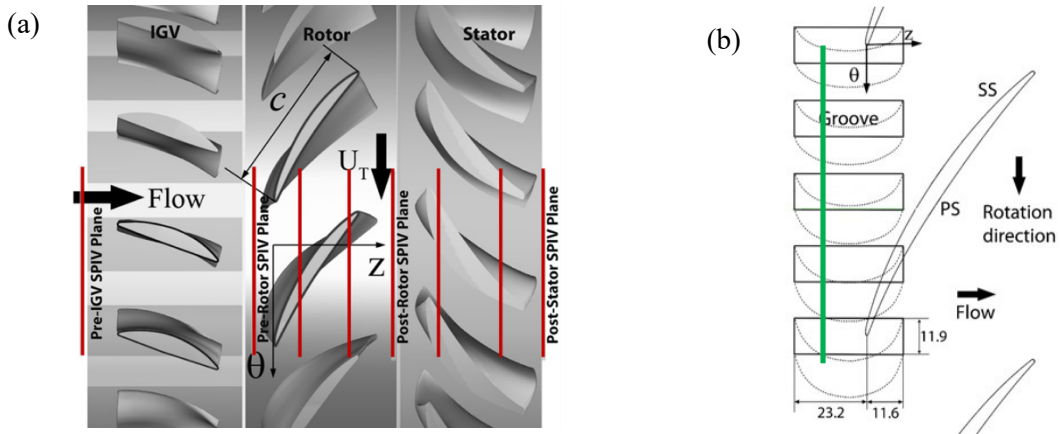


Figure 1.—The locations of (a) axial SPIV planes over the entire machine and (b) the pre-rotor SPIV plane relative to that of the semicircular axial casing grooves.

TABLE I.—LOCATION OF STEREO PARTICLE IMAGE VELOCIMETRY (SPIV) PLANES ILLUSTRATED IN FIGURE 1

SPIV axial plane	Location ^a
Pre-IGV	61 mm upstream IGV LE
Pre-rotor	13 mm upstream rotor tip LE
Through rotor near LE	28 percent rotor axial chord
Through rotor near TE	89 percent rotor axial chord
Post-rotor	17.5 mm downstream rotor tip LE
Through stator near LE	10 percent stator axial chord
Through stator near TE	71 percent stator axial chord
Post-stator	16.5 mm downstream stator TE

^aIGV is inlet guide vane, LE is leading edge, and TE is trailing edge.

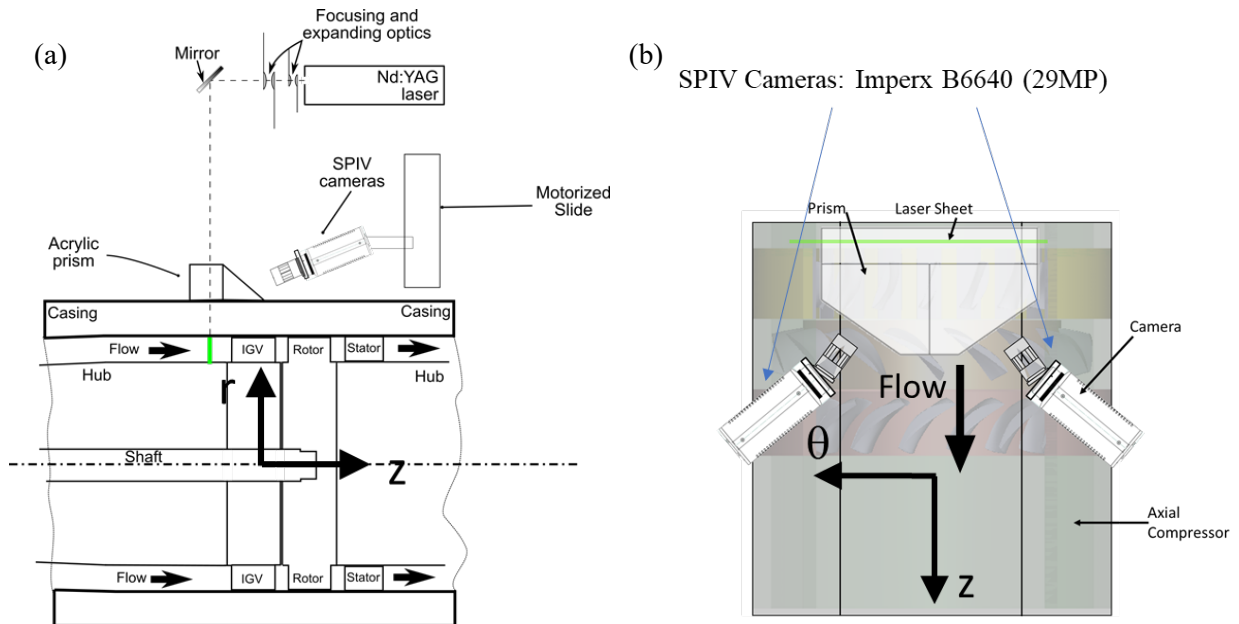


Figure 2.—SPIV setup for the axial plane measurements: (a) Side view. (b) Top view.

2.0 Results: Evolution of the Flow and Reynolds Stresses Across Blade Rows

Preliminary data for the flow in axial planes have been presented at the 2021 Turbo Expo (Ref. 1), and two comprehensive papers have been submitted for inclusion in Turbo Expo 2022 (Refs. 2 and 3). A summary of the findings is presented in Section 2.0 of this report. The mean flow for pre-stall flow rate is presented in Section 2.1, and for the BEP in Section 2.2. Passage-averaged profiles are discussed in Section 2.3. The structure and mechanisms affecting the evolution of turbulence in the passage at pre-stall are discussed in Section 2.4, and close to the BEP in Section 2.5.

2.1 Evolution of the Flow at $\phi = 0.28$: Pre-stall Conditions for Rotor Casings With Untreated Endwalls

2.1.1 Overview

As an overview of the evolution of the flow, Figure 3 compares the axial velocity distributions in the pre-rotor, post-rotor, and post-stator planes under pre-stall conditions (flow rate $\phi = 0.28$) for a smooth, untreated wall (upper row) to those with the ACGs installed (bottom row). The corresponding distributions of circumferential velocity are compared, this time side by side in Figure 4, with the smooth-wall data on the left column, and the semicircular-groove results on the right. At pre-stall condition and without casing grooves, the flow upstream of the rotor shows increased blockage in the tip region distributed over the entire passage. This blockage is associated with the leakage flow, near-circumferential alignment of the TLV, and intermittent rollup of BFVs (Ref. 8) (details follow). As previously discussed, the grooves entrain the TLV, inhibit the BFV formation, and cause periodic variations in flow angle at the leading edge of the blade (Refs. 7 and 21). Furthermore, they homogenize the flow in the passage by generating a series of axially aligned vortices, which entrain high momentum flow from the interior of the passage into the tip region. These vortices form on both sides of the flow jetting out from the upstream end of the grooves (Figure 3(a), and Figure 4(b)). Note that with the grooves, the axial velocity in the passage (U_z) is higher than that without grooves (left column of Figure 3) because of the negative velocity in the grooves, matching the overall flow rate.

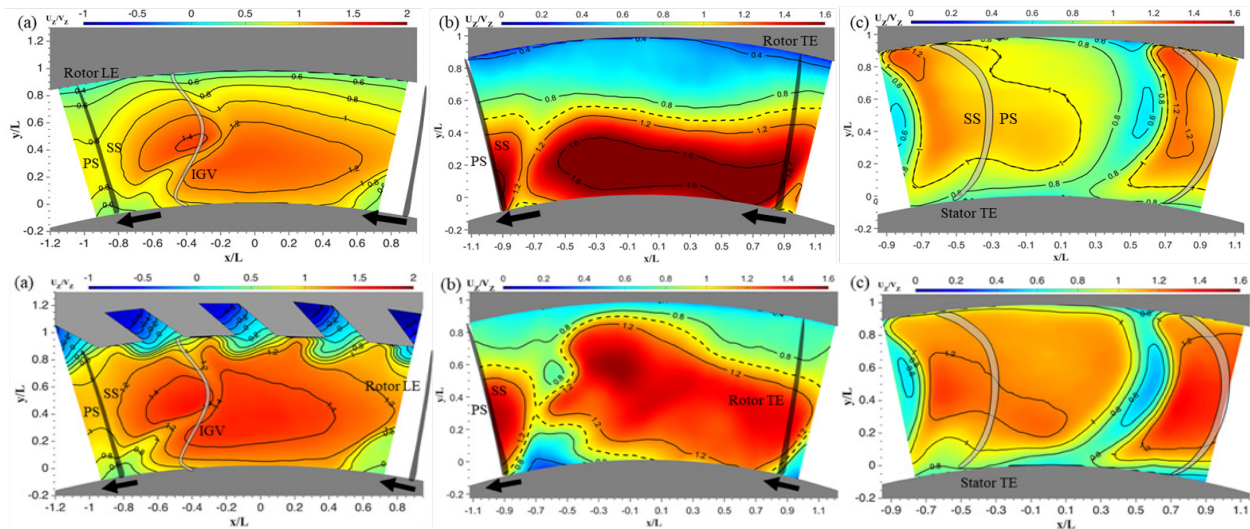


Figure 3.—Evolution of the axial velocity component (normalized by the overall-averaged axial velocity V_z across blade rows). Distribution of axial velocity in the (a) pre-rotor plane, (b) post-rotor plane, and (c) post-stator plane for (top row) without casing grooves, and (bottom row) with the semi-circular grooves installed. Pre-stall flow rate $\phi = 0.28$. Dashed lines in (b) show the location of $U_z/V_z = 1$.

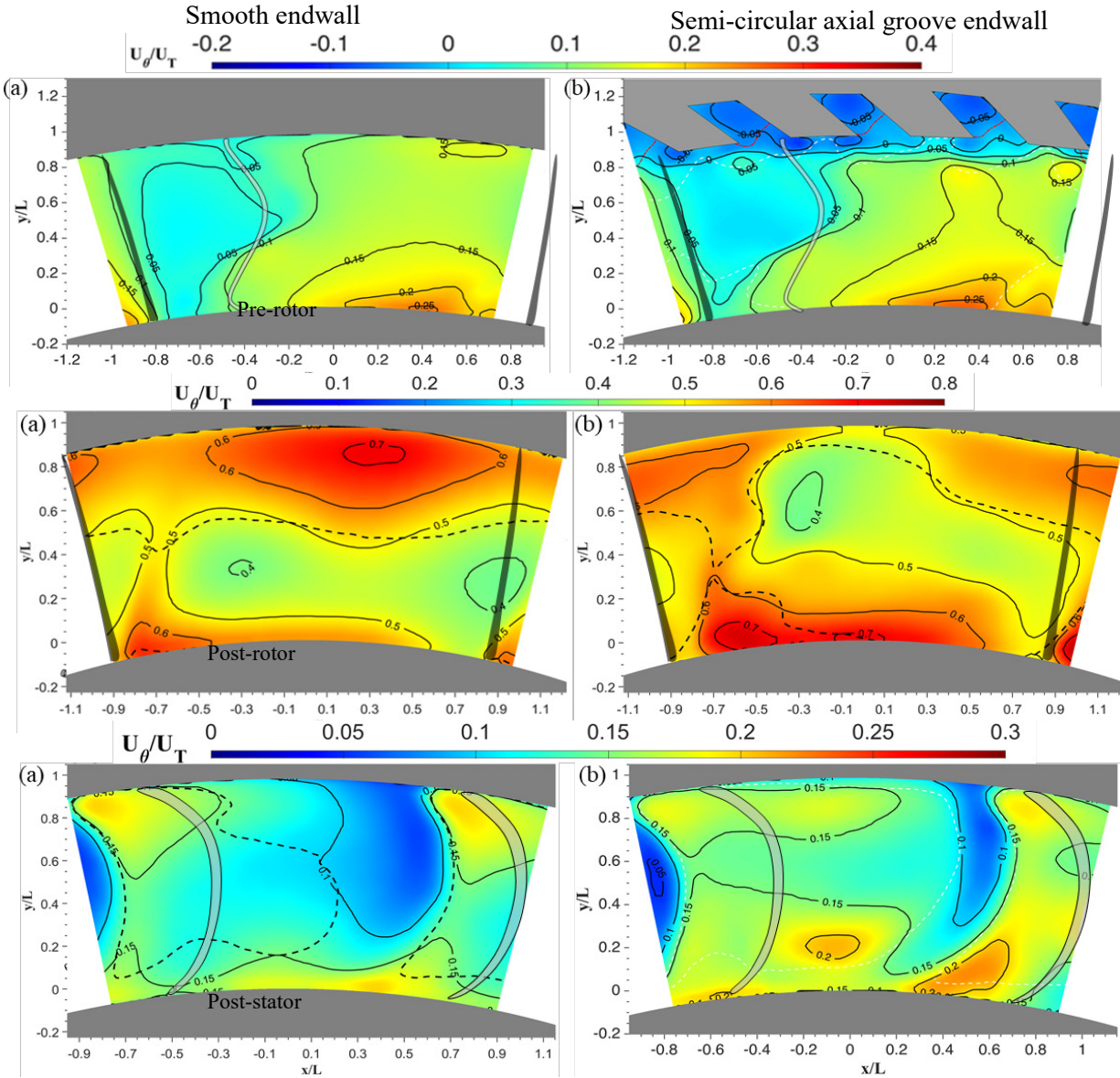


Figure 4.—Distribution of circumferential velocity normalized by the tip speed (U_T) for (a) smooth endwall and (b) semi-circular ACG. Top row: pre-rotor plane, middle row: post-rotor plane, and bottom row: post-stator plane. Pre-stall flow rate. Dashed line shows the location of $U_z/V_z = 1$.

2.1.2 Flow Through the Rotor

Next, the flow structure in each plane is examined in greater detail. Starting with the flow upstream of the rotor, Figure 5 compares the distributions of ensemble-averaged axial velocity, circumferential velocity, and the axial vorticity for the untreated casing to those with the ACGs installed for rotor blade orientation $\Theta = 0^\circ$. The circumferential position of the rotor leading edge (LE), which is located downstream of this plane, is marked on the figure. The axial velocity contours show that the wake of the IGVs, the entire tip region near the casing, and the entire span in front of the blade has low axial momentum. Because of its proximity, the blockage in front of the blade is caused by the presence of the blade LE effect, and it moves circumferentially with the blade as it rotates. The circumferential velocity is relatively higher on the pressure side (PS) of the rotor blade than on the SS, peaking near the PS of the hub. This latter region is observed for each of the four orientations, and it moves with the rotor LE, becoming distorted when the rotor blade is in

the vicinity of the IGV wake, such as for the shown orientation. The distribution of axial vorticity has the in-plane velocity vectors diluted by 2:1 in the radial direction (for clarity) superimposed on it. The most notable feature in the vorticity distribution is the clear signature of the IGV wake with a high negative peak in the middle of the passage.

The second row of Figure 5 shows the same distributions with the ACGs installed. The SPIV plane cuts the grooves close to their upstream end. Here, the axial velocity inside the grooves is mostly negative (Figure 5(d)), as expected. Near the endwall, in the region where the outflow from the grooves jets out into the passage, the axial velocity is low, but it is high in the space between grooves. The negative axial flow inside the grooves is accompanied by an elevated axial velocity deep in the passage compared to that of the untreated casing. Because of the groove orientation, the outflow from the grooves has a negative circumferential direction, creating a layer of $U_\theta < 0$ along the tip region. Since the main passage flow below this layer has a circumferential momentum in the direction of blade rotation, there are significant radial gradients of circumferential velocity in this region, hence the layer with elevated negative vorticity. In addition, the flow jetting out of the grooves generates pairs of axially aligned vortices on the corners of the grooves (Figure 5(f)). Although the vortex pairs always appear irrespective of the rotor blade orientation, the strengths of these vortices vary. The positive radial velocity induced by these vortices in the space between grooves entrains high axial momentum fluid from inner parts of the passage to the tip region, reducing the blockage there. This effect of semicircular ACGs had not been recognized in our earlier studies based on observations in meridional planes.

Whereas the mean axial velocity for the untreated casing is positive over the entire plane upstream of the rotor, the instantaneous realizations in Figure 6(a) show frequent appearances of regions with negative axial velocity. They are almost always surrounded by regions of fast outward flow away from their center (like a source), giving an impression of a flow circumventing a region with high adverse pressure gradients. Figure 6(b) and (c) provide statistics on the circumferential and radial locations of these reverse axial flow events, respectively, for four different rotor blade orientations based on analysis of 2,000 instantaneous realizations. The radial distribution (Figure 6(c)) shows that such events are restricted to the top 30 percent of the passage, with about 50 percent of them occurring in the tip gap region. While these events occur at all circumferential locations, they are preferentially located in front of the blade and biased towards the PS, irrespective of blade orientation. The preferential alignment with the LE is presumably affected by the blade-induced pressure gradients. The preferred presence on the PS is consistent with the region where backflow vortices (BFVs), which extend diagonally upstream from the midchord SS of one blade to the PS near the LE of the next blade (see cavitation visualization image in Figure 7(d)). The impact of the IGV wake on the occurrence of reverse flow events can be seen by comparing the area fraction of these events—that is, their area over the entire investigated area over all realizations—for the four blade orientations (Figure 6(d)). As is evident, the area fraction is 75 percent larger when the rotor blade PS is located in the vicinity of the IGV wake, for $\Theta = 0^\circ$ and 4.8° .

To further highlight the role of BFVs in inducing intermittent reverse flow upstream of the rotor, Figure 7(a) and (b) show sample contour plots of the instantaneous realization of axial velocity and circumferential vorticity, respectively, in a meridional plane located close to the rotor blade tip LE ($z/c_a = 0$, indicated by dotted lines; c_a is the axial chord length), shortly before the blade reaches the sample plane (see Figure 7(c)). The sample area contains a large vortex whose center is marked with a black arrow in Figure 7(b), extending upstream of the LE plane and inducing a negative axial velocity above its center up to $z/c_a = -0.13$. The location, orientation, and negative velocity induced by this vortex on the PS of the blade are consistent with that of BFV, as demonstrated by the cavitation flow visualization image in Figure 7(d). Multiple such structures form in the untreated passage, and they can induce reverse flow at multiple locations in the passage, preferentially on the PS (Figure 6(b)).

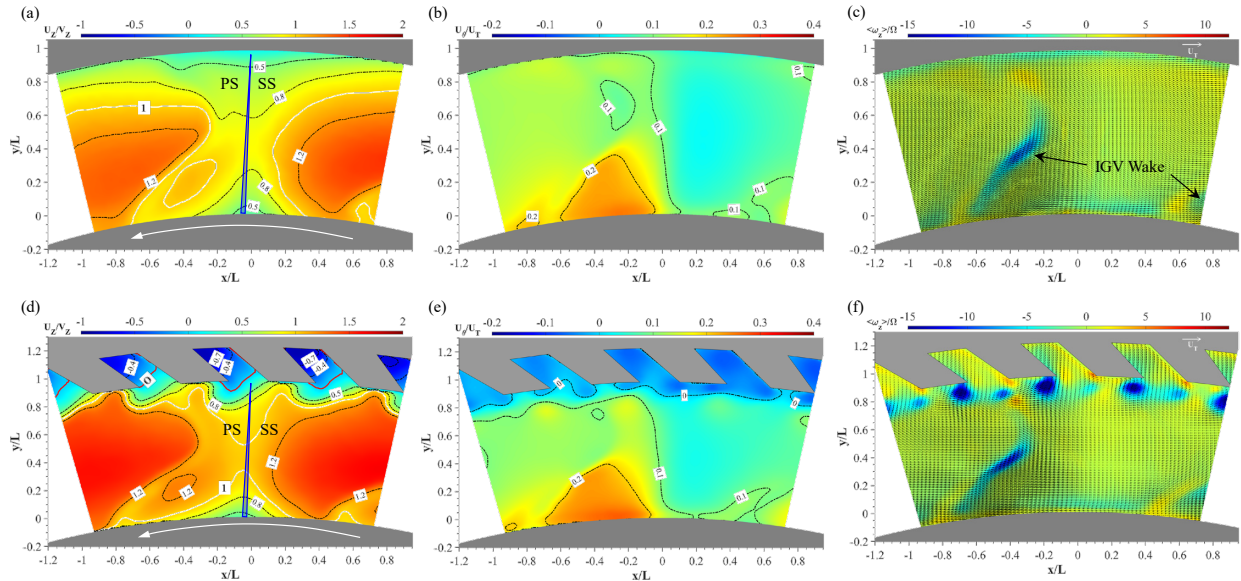


Figure 5.—Ensemble-averaged distributions upstream of the rotor at $\phi = 0.28$. First row: Untreated casing, second row: ACGs. (a,d) Axial velocity (U_z/V_z). (b,e) circumferential velocity (U_q/U_T), and (c,f) axial vorticity ($\langle \omega_z \rangle / \Omega$). Solid white lines are contours of $U_z/V_z = 1$; solid red lines are contours of $U_z/V_z = 0$.

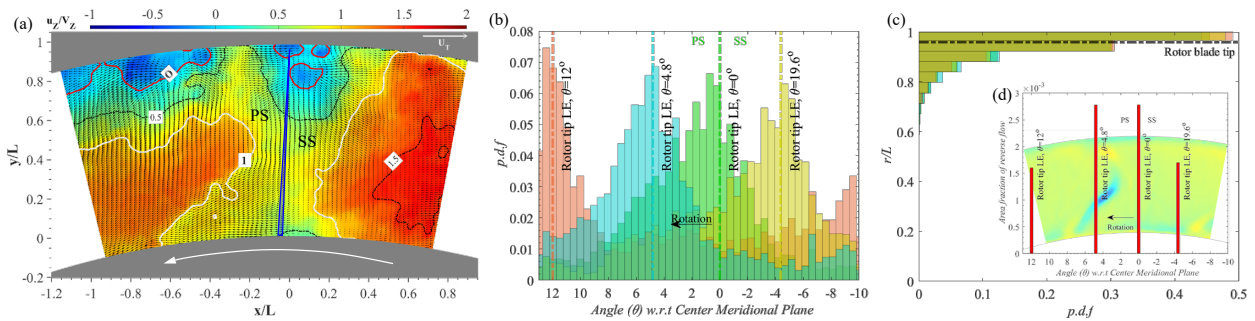


Figure 6.—(a) Sample of instantaneous velocity field showing a reverse axial flow blockage event upstream of the rotor, (b) circumferential distribution of the location of $U_z < 0$ (blockage) events with the corresponding rotor blade location shown in the same color, (c) radial distribution of blockage events, and (d, inset) area fraction of blockage events for the four rotor blade orientations overlaid on color contours of axial vorticity.

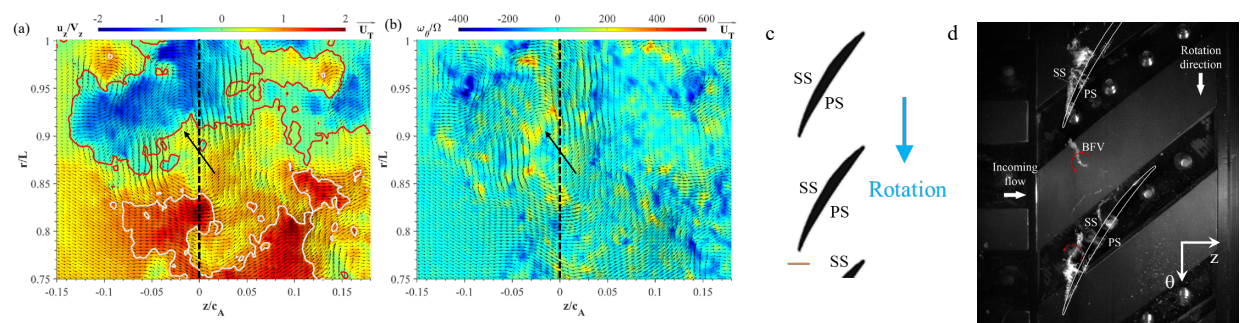


Figure 7.—Instantaneous realization showing a reverse flow event in a meridional plane at $s/c = -0.11$ for an untreated endwall casing. (a) Axial velocity contours superimposed on the in-plane velocity vectors, (b) corresponding circumferential vorticity, (c) location of meridional plane relative to the rotor blade, and (d) sample cavitation visualization showing the orientation of a BFV and a TLV.

The evolution of the ensemble-averaged flow inside the untreated rotor passage is summarized in Figure 8. At $z/c_a = 0.28$, the blockage region with low U_z and high U_θ (peaking as high as 80 percent of the tip speed) extends to the upper 30 percent of the passage. Here, the axial velocity is negative near the endwall casing along the entire circumference, presumably under the influence of the TLV, BFV, and reverse leakage flow (details follow). At $z/c_a = 0.89$, the blockage region expands to about 40 percent of the passage, but the negative velocity region is restricted mostly to the blade tip and the SS of the rotor. Downstream of the blade, the low U_z and elevated U_θ region covers about 50 percent of the blade span.

The axial vorticity ($\langle \omega_z \rangle$) is negative in thin layers along the outer casing and positive over a broad area in the middle of the span. Both layers are predominantly associated with radial gradients in U_θ . To explain how these layers are related to the tip region flow structure, refer to results of prior measurements in a meridional plane of the same machine and flow conditions as studied in Reference 8. Figure 9(a) shows the axial vorticity distribution, and Figure 9(b) illustrates the multilayer vortical structure around the TLV center overlaid on the circumferential velocity distribution. They show that the tip leakage flow, the TLV, and the flow surrounding it appear like a swirling jet that rotates in the same direction as the blade, but at a lower velocity than the tip speed. As the entrained leakage flow with elevated U_θ swirls around the TLV center, the negative axial vorticity layer (where $\partial U_\theta / \partial r < 0$) flowing across the tip gap from the pressure side (Layer 1) changes first to a radial vorticity layer, and then to a broad positive axial vorticity layer ($\partial U_\theta / \partial r > 0$) below the TLV center (Layer 4). The signatures of these two layers are evident in the axial planes depicted in Figure 8. Layer 2 cannot be seen in the axial planes data (Figure 8(c)), presumably since this layer is too thin at $z/c_a = 0.28$ for the resolution of the axial plane measurements, which cover the entire passage (vector spacing of 0.64 mm, requiring 1.9 mm for measuring spatial derivatives). Hence, Layers 1 and 3 (Figure 9(a)) appear as one negative $\langle \omega_z \rangle$ layer. Deep in the passage ($z/c_a = 0.89$, third row of Figure 8), entrainment and generation of secondary vortical structures, most prominently the BFVs, persist. They cause TLV breakdown (Ref. 8) and expand radially inward to a substantial fraction of the passage span. Consequently, the positive axial vorticity layer becomes broad while the negative layer remains confined to the tip region. The broad positive layer persists, albeit at a lower magnitude, downstream of the rotor (third row of Figure 8).

Finally, it would be worthwhile to demonstrate the striking level of flow instability in the rotor passage under pre-stall conditions. Sample instantaneous velocity and vorticity distributions $z/c_a = 0.28$ are presented in Figure 10. The region with $U_z < 0$ extends to the midspan, the peaks in U_θ exceed the blade tip speed, and the axial vorticity with distinct peaks associated with the backflow vortices is distributed across the entire width of the passage. Further downstream (not shown), as the positive vorticity layer expands, some of these vortices intermittently reach the rotor hub. The associated turbulence level is extremely high, as discussed later in this report (and in Koley et al. (Ref. 3)). The negative vorticity peak near the casing is presumably associated with the TLV.

The flow structure downstream of the rotor changes drastically when the axial casing grooves are installed, as demonstrated by direct comparisons in Figure 3 and Figure 4 for one of the rotor orientations, and in Figure 11 for another orientation. The latter matches the phase of the rotor in the bottom row of Figure 8, so distributions can be compared directly. Measurements were planned to be taken in planes intersecting with the rotor passage as well, similar to those recorded for the untreated machine, but there was no time. It is hoped these measurements will be made in the future. As is evident, with the grooves installed, the size of the region with low axial momentum and elevated circumferential velocity in the tip region decreases significantly. Here, apart from the blade wake, the low-momentum region is mostly centered near the PS of the blade wake. This pattern rotates with the rotor, as can be readily observed by a comparison to Figure 3 and Figure 4. It appears to be affiliated by the TLV and BFVs generated by the previous blade (to the left side of the field of view), which migrate to the PS of the next blade.

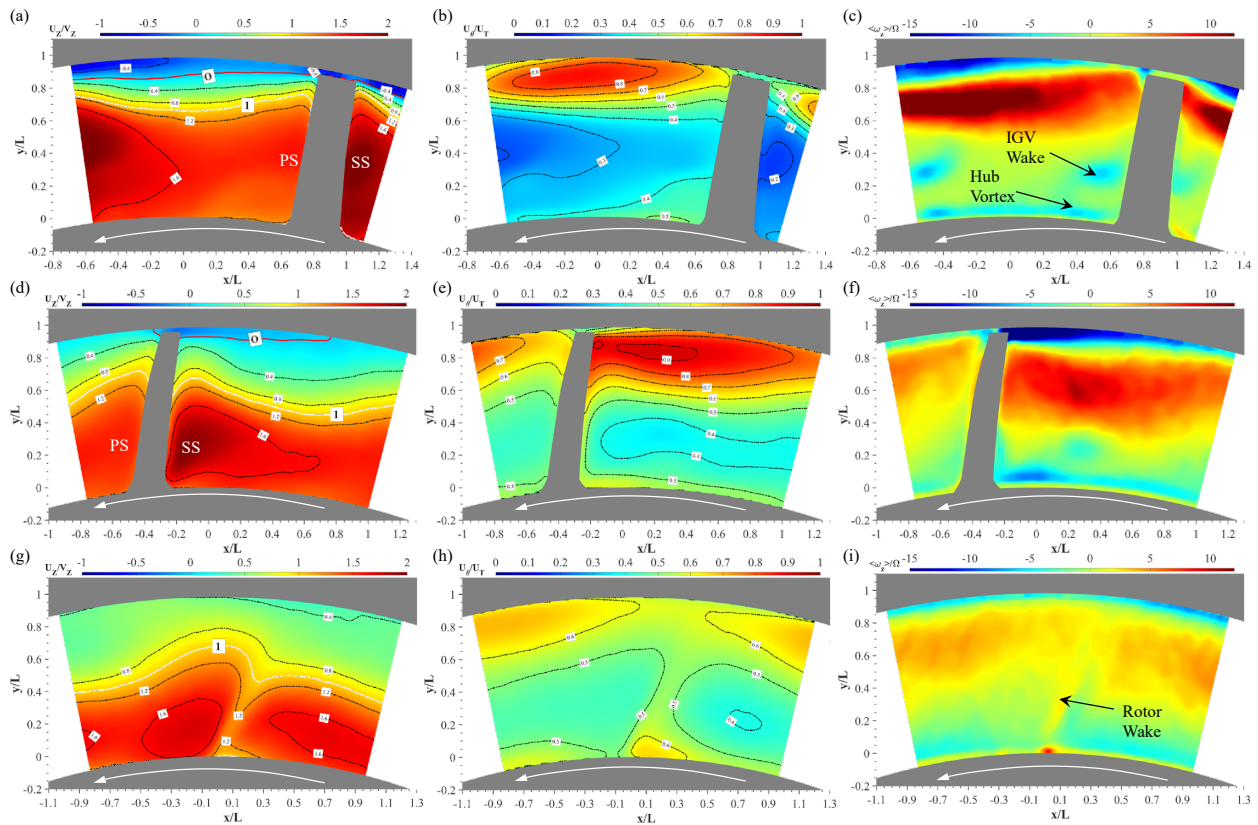


Figure 8.—Evolution of the flow in the rotor with untreated endwall at $\phi = 0.28$ and $\Theta = 0^\circ$. Distribution of ensemble-averaged (left column, a,d,g) axial velocity, (middle column, b,e,h) circumferential velocity, and (right column, c,f,i) circumferential vorticity. Top row: $z/c_a = 0.28$, middle row: $z/c_a = 0.89$, and bottom row: downstream of the rotor. White lines: $U_z/V_z = 1$; red lines: $U_z/V_z = 0$.

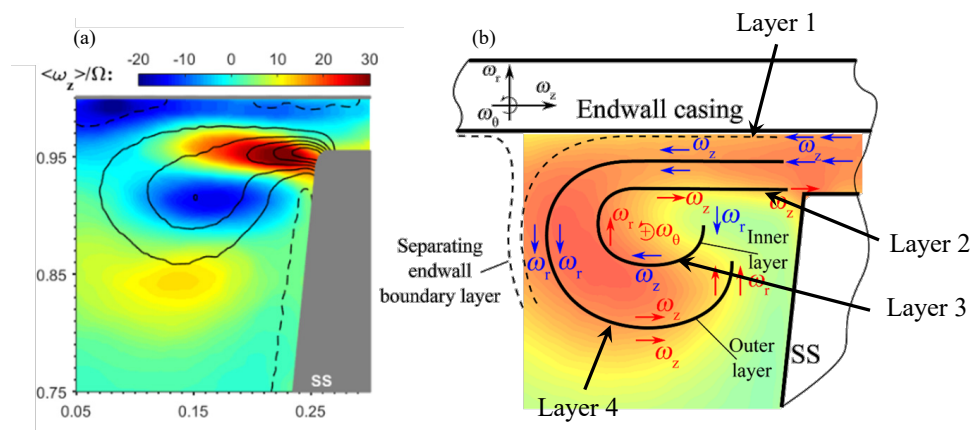


Figure 9.—(a) Axial vorticity distribution and (b) illustration of the multilayer vorticity structure superimposed on the circumferential velocity distribution in a meridional plane of the same compressor and flow conditions as Huang et al. (Ref. 8).

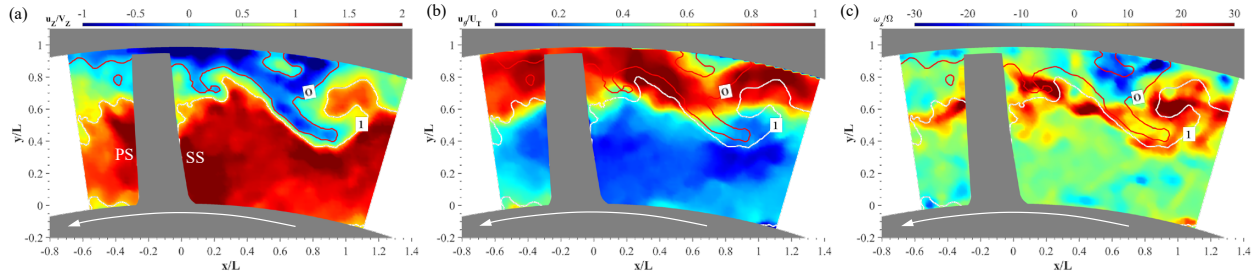


Figure 10.—Sample instantaneous distributions of (a) axial velocity, (b) circumferential velocity, and (c) axial vorticity, demonstrating the flow instability in the rotor passage at $z/c_a = 0.28$ and $\phi = 0.28$ with untreated casing.

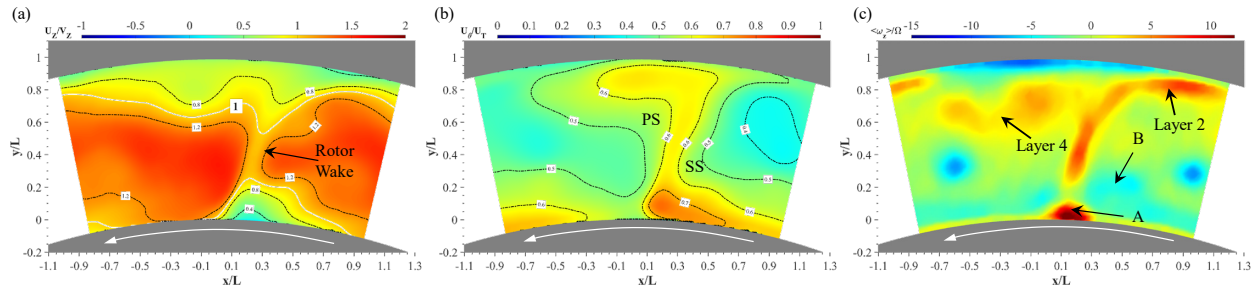


Figure 11.—Ensemble-averaged distributions of (a) axial velocity, (b) circumferential velocity, and (c) axial vorticity downstream of the rotor for $\phi = 0.28$ with the casing grooves installed.

Although part of the TLV is entrained into the groove, and generation of BFVs is prevented near the leading edge, both vortices continue to form downstream of the groove, but to a limited extent. Hence, their scales and impact on the flow structure are significantly weaker than those occurring near the untreated endwall. Near the endwall, there are two separate circumferentially aligned layers of positive vorticity on either side of the wake. On the PS, the layer is located under the TLV and appears to correspond to Layer 4 in Figure 9 (meridional view) for the untreated endwall. On the SS, the layer that appears to merge with the blade corresponds to Layer 2 in Figure 9. Next, near the hub on the SS, there is a region of high positive vorticity (marked “A” in Figure 11(c)) that has a mild negative region above it (marked “B”). Although the origin of these regions cannot be pinpointed, it is possible that the $\langle \omega \rangle > 0$ peak is associated with the hub/horseshoe vortex leg propagating along the SS of the blade, and the broad negative region is the hub vortex leg that originated from the pressure side of the neighboring blade. Both can be seen also in the results for the untreated endwall (Figure 8(i)), but with lower magnitudes. The blade wake signature is more distinct with the grooves. Its positive vorticity is mostly associated with circumferential gradients of radial velocity (not shown). Finally, the two nearly circular blobs of negative vorticity in the middle of the passage are the signatures of the IGV wake (see Figure 5(f)), implying the IGV-induced flow non-uniformities persist downstream of the rotor. For the untreated endwall and at pre-stall conditions, these signatures can be seen at $z/c_a = 0.28$, but not further downstream, presumably since they are scrambled by the high turbulence in the rotor passage.

2.1.3 Flow In and Downstream of the Stator

The evolution of flow in the stator passage for the entreated endwall is presented in Figure 12. Note that the color scales here are different from those in the rotor passage and in some cases vary across planes. The broad layer with low axial momentum downstream of the rotor extends into the beginning of the stator ($z/c_a = 0.1$ in Figure 12(a)). In this region, U_θ is still elevated in the outer parts of the stator

passage (Figure 12(b)), but not to the same extent as in the rotor. Deeper into the stator (Figure 12(d), second row, $z/c_a = 0.71$) the axial velocity distribution becomes more homogenized, and the elevated circumferential velocity region shrinks (Figure 12(e)). The elevated vorticity layer also fades. Downstream of the stator, U_z (bottom row, Figure 12) shows limited signs of the earlier momentum deficit in the outer layer, but there is a broad area with low axial momentum and nearly zero circumferential velocity in the stator blade wake. While the mean boundary layer on the stator blades remains attached in the aft part of the stator passage (U_z remains positive in Figure 12(d)), instantaneous realizations (not shown) indicate that boundary layer separation occurs intermittently in lower sections of the aft part of the stator SS, generating a negative flow there and, inherently, an increase in the turbulence level. This process is presumably caused by the adverse pressure gradients on the stator, as evidenced by the rapid decrease in U_z from U_z/V_z of >1.7 at $z/c_a = 0.1$ to 0.4 at $z/c_a = 0.71$ along the inner part of the SS boundary layer. Consequently, the stator blade wake is broad and is characterized by low axial and circumferential velocity throughout the span. Finally, the stator in this machine has a rotating hub, and the blades are cantilevered with a measured tip gap of about 0.6 mm; that is, it is much narrower than the rotor tip gap. Hence, the details of the hub leakage flow are not resolved at the present magnification. However, the flow structure near the hub, consisting of low axial velocity and elevated circumferential velocity, is consistent with the trends observed for the rotor tip leakage.

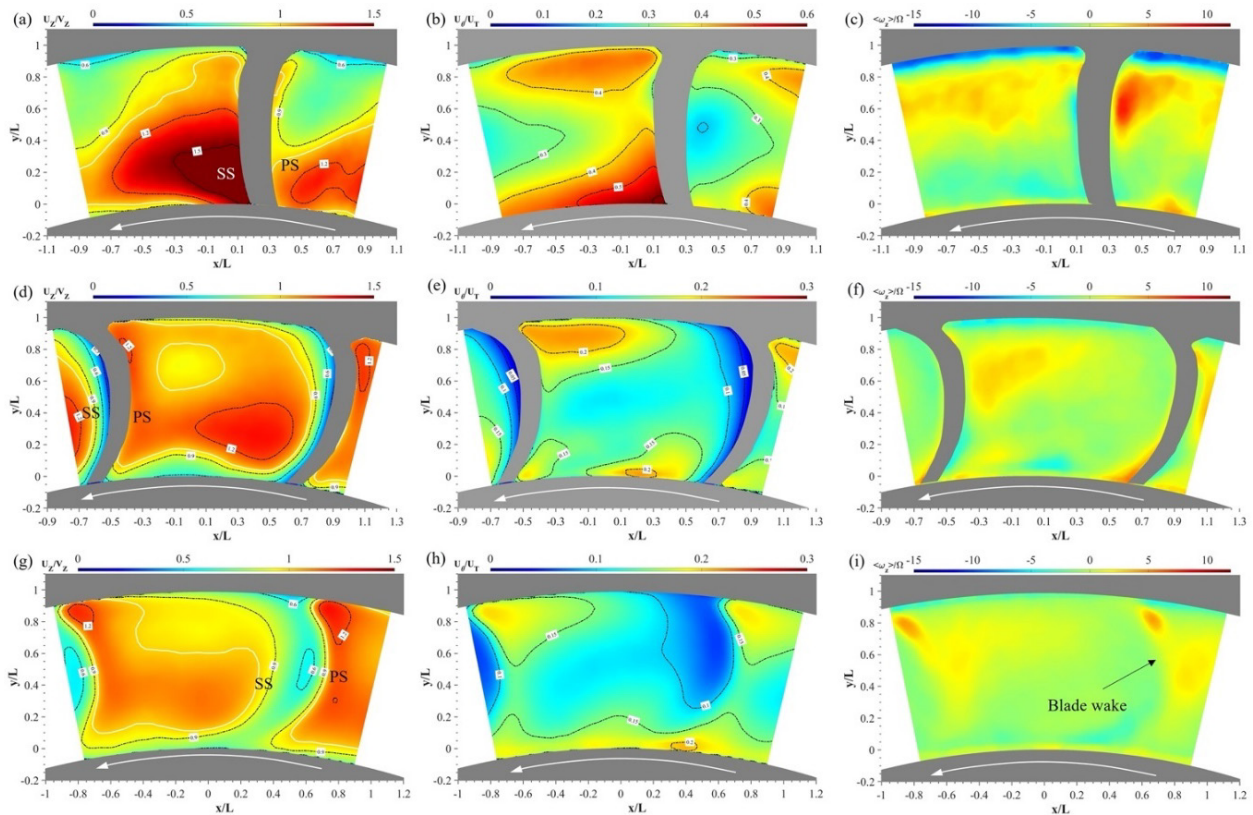


Figure 12.—Evolution of the flow in the stator for the untreated endwall at $\varphi = 0.28$ and $\Theta = 0^\circ$. Distribution of ensemble-averaged (left column, a,d,g) axial velocity, (middle column, b,e,h) circumferential velocity, and (right column, c,f,i) circumferential vorticity. (Top row, a,b,c) $z/c_a = 0.10$, (middle row, d,e,f) $z/c_a = 0.71$, and (bottom row, g,h,i) downstream of the stator. White lines: $U_z/V_z = 1$.

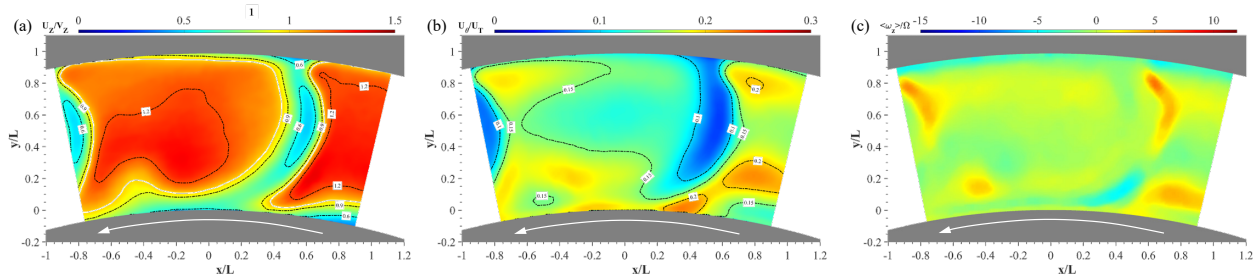


Figure 13.—Ensemble-averaged distributions of (a) axial velocity, (b) circumferential velocity, and (c) axial vorticity downstream of the stator for $\phi = 0.28$, with the casing grooves installed.

The velocity distributions downstream of the stator with the axial casing groove installed is shown in Figure 13. Compared to the results for the untreated endwall casing, the axial velocity distribution here (Figure 13(a)) is more homogenous, and the stator wake is distinctly thinner. The latter is also evident from the distribution of U_θ (Figure 13(b)). The thinner wake should be an expected outcome of the reduced U_z at the entrance to the stator in the inner part of the passage (compare Figure 8(a) and Figure 11(a)). Consequently, the flow deceleration, hence the adverse pressure gradients in the inner part of the passage, are expected to be milder. In the vorticity distributions (Figure 13(c)), the signatures of stator blade wakes are more distinct along with the hub flow structures. The negative vorticity on the SS and positive peak on the PS could be related to hub vortices, but the flow there is also affected by leakage flow, which is not resolved at the present spatial resolution. Measurements should also be performed in planes intersecting with the stator blade and a higher magnification to resolve the flow in and around the hub gap.

2.2 Mean Flow Structure Near the Best Efficiency Point ($\phi = 0.37$)

The axial and circumferential velocity distributions upstream of the rotor close to the BEP are shown in Figure 14. For a smooth endwall, the axial momentum (Figure 14(a)) is low near the casing, in the hub, in front of the blade LE, and at the intersection of the IGV wakes and rotor blade with the hub. However, the velocity deficits, especially in the tip region, are considerably milder than those occurring under pre-stall conditions (Figure 5(a)). Consequently, the axial velocity in the middle of the passage is lower. In contrast, the circumferential velocity at the BEP (Figure 14(b)) is higher than at that at pre-stall over the entire passage although their spatial distributions appear to be similar. Unlike the pre-stall flows, there are no regions or events of negative axial velocity in the instantaneous realizations since a significant fraction of the TLV rollup occurs further downstream, the leakage flow is considerably weaker (Ref. 13), and the BFVs are less frequent and do not extend to the PS of the next blade. With the ACGs installed (Figure 14(c) and (d)), the axial and circumferential velocity components in the grooves are negative, as expected, but their magnitudes are lower than those at pre-stall. The flow still jets out of the grooves and generates the pair of axial vortices along the sides of each groove (not shown), but the velocities involved are lower; hence, their influence on the flow structure in the tip region is reduced.

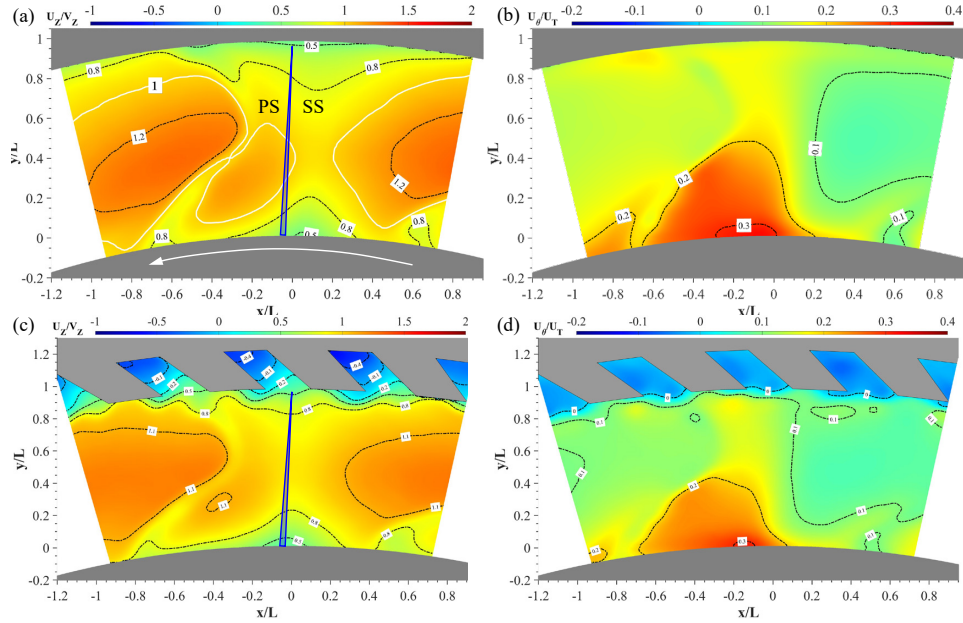


Figure 14.—Ensemble-averaged flow structure upstream of the rotor near BEP at $\phi = 0.37$; (First row, a,b) for the untreated endwall and (second row, c,d) axial casing installed. (Left column, a,c) U_z/V_z and (right column, b,d) U_θ/U_T .

The evolution of velocity and axial vorticity distributions across the rotor passage are presented in Figure 15. Clearly, the axial velocity deficits are significantly smaller than those at pre-stall and are mostly confined to the tip region. The elevated U_θ region is also narrower and does not extend circumferentially to the entire passage (Figure 15(b), (e), and (h)). The signature of the leakage flow near the SS of the blade tip with negative axial and circumferential velocity components is also evident. The vorticity map at $z/c_a = 0.28$ (Figure 15(c)) shows multiple negative peaks, with the most prominent being the signatures of the TLV of the shown blade near the SS tip and that of a previous blade on the left side. Other regions include the PS corner of the blade tip, which is associated with the leakage flow entering the tip gap, two midpassage peaks originating from the IGV wakes, and two structures near the hub. One of these is presumably associated with the rotor blade hub vortex on the pressure side, and the other is likely to originate from the IGV. Positive axial vorticity peaks are present in two distinct regions. The first extends from the blade tip to the TLV and is presumably associated with the Layer 2 illustrated in the meridional view (Figure 9(b)). The second region is located to the right of the TLV of the previous blade and is associated with the region of radial U_θ gradients on the outer side of the TLV (upstream of the TLV in the meridional view).

Deeper in the passage, the TLV, the leakage flow, and the region with elevated U_θ extend away from the SS of its originating blade towards the PS of the next blade (Ref. 13). At $z/c_a = 0.89$, the TLV is located at x/L of ~ 0.7 , near the leftmost point of the layer with negative axial vorticity (Layer 3 in Figure 9(b)). It is bounded by two layers of positive vorticity, a narrow layer close to the tip, and a broader layer, where U_θ is high, deeper in the passage (where BFVs roll up). These layers are mostly affected by radial gradients in U_θ , and are identified as Layers 2, 3, and 4 in the meridional plane shown in Figure 9. The negative vorticity layer extends diagonally to the outer casing, where it persists all the way to the PS of the next blade, as seen on the left side for a previous blade. This latter layer corresponds to Layer 1 in Figure 9(b). Downstream of the rotor (3rd row of Figure 15), the remnants of positive vorticity Layer 2 merge with the rotor wake, and those of positive Layer 4 associated with the previous

blade are visible on the PS of the wake. A thin region with negative $\langle \omega_z \rangle$ along the casing appears to be the remnants of Layer 1. A faint peak appears to be the leftover of Layer 3 and the TLV. The broad negative vorticity region on the SS of the wake and close to the hub appears to originate from the hub vortex of the next blade to the right, as discussed earlier for the cases with ACGs at $\phi = 0.28$ (Figure 11).

With the ACGs installed (Figure 16), for the most part, the axial and circumferential velocity distributions downstream of the rotor appear to be very similar to those of the untreated endwall (compare to Figure 15(g), (h), and (i)). However, the region with reduced axial velocity and elevated U_θ appears to be more circumferentially distributed. The vorticity distributions are also quite similar, although the TLV signature at the left end of the negative vorticity layer is less distinct. As discussed in Reference 7, at high flow rates a fraction of the TLV is entrained into the groove, and the rest, along with the part that rolls up downstream of the grooves, becomes distributed over a broader area due to interaction with secondary structures entrained from the grooves.

Finally, with similar flow structures at the exit from the rotor, the velocity and vorticity distributions downstream of the stator with the casing grooves are very similar to those of the untreated endwall. The axial velocity distribution for the smooth endwall is presented in Figure 17. Except for deficits near the hub, the narrow stator blade wake, and very close to the endwall, the streamwise momentum distribution is uniform. The circumferential velocity distribution (not shown) is also quite uniform, with magnitudes ranging from $0.15U_T$ to $0.30U_T$.

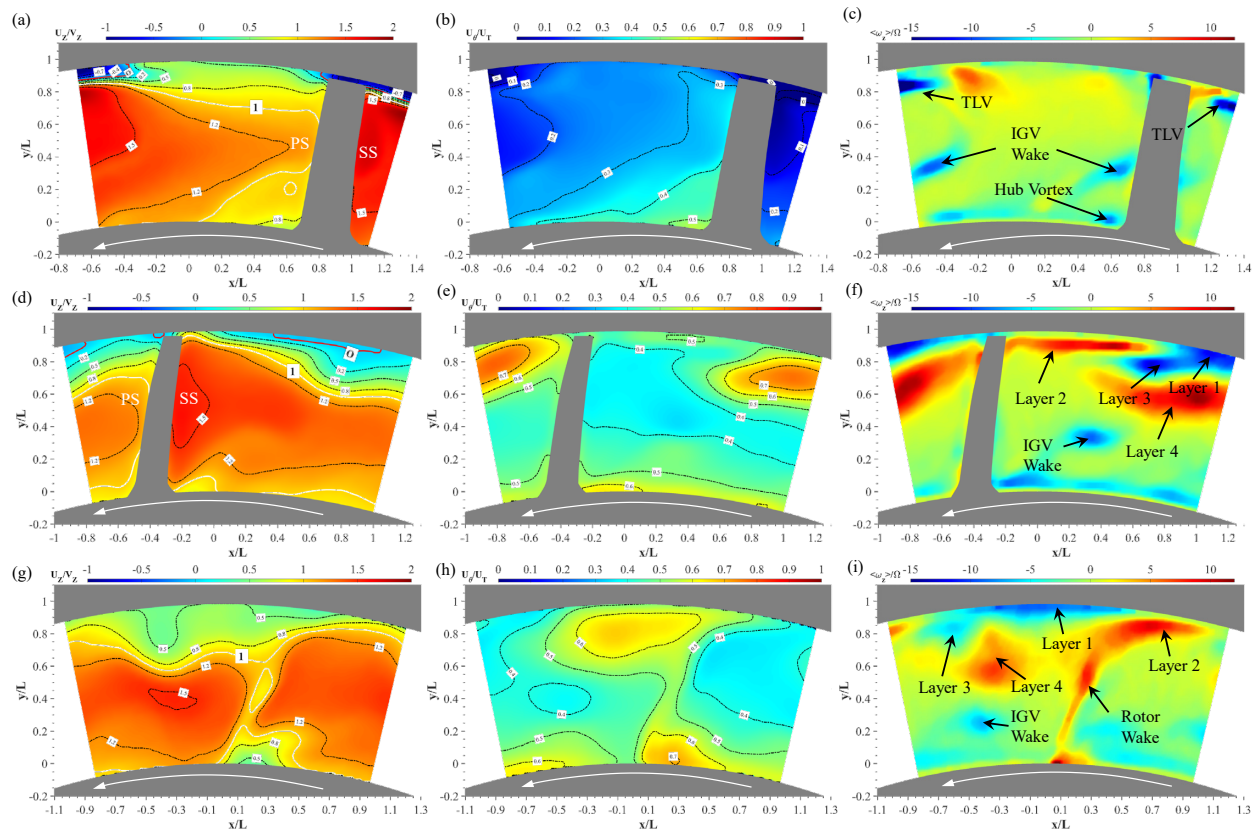


Figure 15.—Evolution of the flow in the rotor with untreated endwall near BEP (at $\phi = 0.37$) for rotor blade orientation of $\Theta = 0^\circ$. Distribution of ensemble-averaged (left column, a,d,g) axial velocity, (middle column, b,e,h) circumferential velocity, and (right column, c,f,i) circumferential vorticity. (Top row, a,b,c) $z/c_a = 0.28$, (middle row, d,e,f) $z/c_a = 0.89$, and (bottom row, g,h,i) downstream of the rotor. White lines: $U_z/V_z = 1$; red lines: $U_z/V_z = 0$.

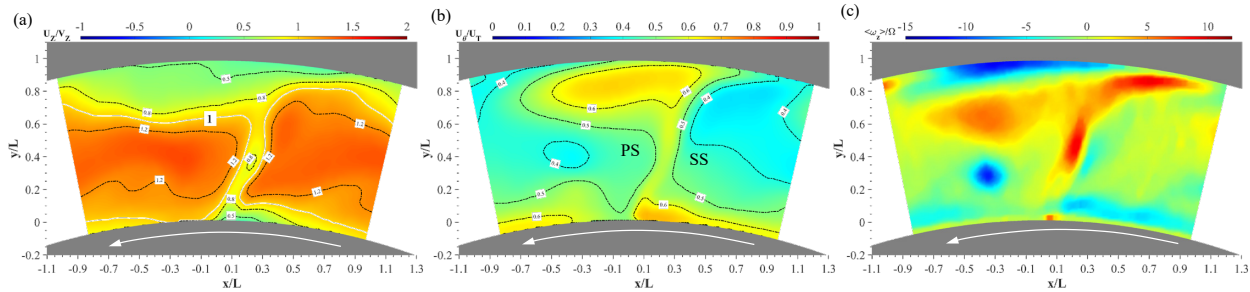


Figure 16.—Flow downstream of the rotor at $\phi = 0.37$ with the casing groove installed. Ensemble-averaged distributions of (a) axial velocity, (b) circumferential velocity, and (c) axial vorticity.

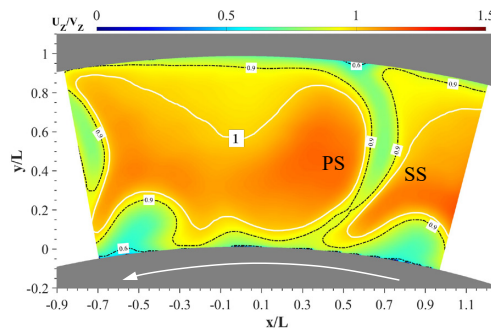


Figure 17.—Ensemble-averaged axial velocity U_z/V_z downstream of the stator with untreated casing at $\phi = 0.37$.

2.3 Passage-Averaged Velocity Profiles

To further evaluate the impact of operating condition and ACGs on the flow structure, the data have been integrated circumferentially to obtain the passage-averaged velocity profiles for all four rotor blade orientations in the IGV-rotor gap, rotor-stator gap, and downstream of the stator. The results are presented in Figure 18. Here, the axial velocity profiles are normalized by the passage-averaged axial velocity V_{zp} in the passage area being averaged. It differs from the annual area mean velocity V_z by 2 to 3 percent, 5 to 6 percent, and 2 to 3 percent in the pre-rotor, post-rotor, and post-stator planes, respectively, presumably due to circumferential variations in fluxes. The left column shows U_z/V_{zp} , and the right column, U_θ/U_T . For all cases and most locations, the blade orientation has very little impact on the passage-averaged velocity profiles. The only exceptions are the reverse flow profiles within the grooves upstream of the rotor at $\phi = 0.28$ (Figure 18(a)). In this case, the orientation of the blade relative to the IGV blades seems to affect the reverse flow from the grooves.

Upstream of the rotor (Figure 18(a) and (b)) and at pre-stall, the axial velocity with ACGs is higher than that of the untreated endwall over the entire span due to the reverse flow in the grooves (the overall mean is the same). In contrast, differences in the circumferential velocity are confined to the top 20 percent of the passage. At the BEP, the negative axial velocity in the groove has a lower magnitude compared to that at pre-stall; hence, the elevated axial velocity in the passage is also lower and differs from that of the untreated endwall only in the outer part of the passage. Conversely, the grooves reduce the circumferential velocity throughout the entire span (Figure 18(b)), demonstrating that the impact of groove is not confined to the tip region.

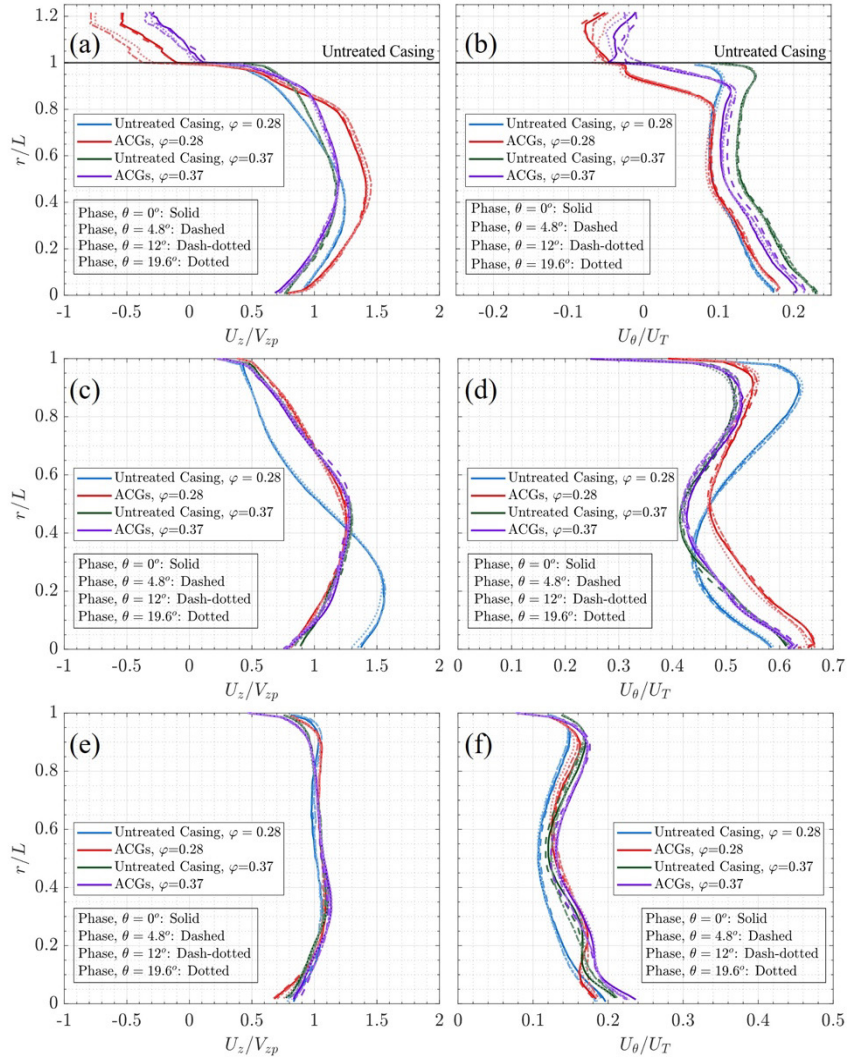


Figure 18.—Passage-averaged velocity profiles for the four rotor blade orientations, with and without axial casing grooves. (Left column, a,c,e) U_z/V_{zp} and (right column, b,d,f) U_θ/U_T . (a,b) Upstream of the rotor, (c,d) rotor-stator gap, and (e,f) downstream of the stator.

In the rotor-stator gap Figure 18(c) and (d) show that most of the axial velocity profiles nearly collapse except for the untreated endwall low flow rate case. The latter has a nearly 50 percent velocity deficit near the tip, and a substantially higher velocity in the inner part of the passage. The corresponding circumferential velocity is high in the tip and hub regions, consistent with the trends discussed earlier. With the grooves and at $\phi = 0.28$, the axial velocity in the upper part of the span is slightly higher than that at high flow rate, possibly due to greater ingestion of the TLV into the grooves. The grooves also significantly reduce the circumferential velocity over the entire outer part of the passage, but increase it near the hub, again affecting the entire span. At the BEP, all of the U_z and U_θ profiles collapse.

The profiles downstream of the stator (Figure 18(e) and (f)) display more uniformity and considerably lower differences among the different cases. The axial velocity profiles nearly collapse, although both the high flow rate cases have slightly lower velocity near the tip, and higher velocity midspan. The slightly lower axial velocity at midspan for the untreated endwall and $\phi = 0.28$ corresponds to the widened velocity deficit in the blade wake. The corresponding U_θ is also lower than those of the other cases,

because of the low circumferential flow within the wake (see Figure 12(h)). Yet, despite the intermittent separation on the stator blade boundary layer, the stator is an effective flow homogenizer, even without casing grooves. The signature of this reduced stability is seen in the wide wake signature downstream of the stator row. As previously discussed, with the grooves, the axial velocity near the hub upstream of the stator is reduced significantly; hence, the deceleration in the stator passage is milder, the SS boundary layer stabilizes, and the blade wake are thinner. Clearly, the grooves located upstream of the rotor modify the flow structure downstream of the stator. Near the BEP, the flow downstream is highly homogenized and is very similar with and without the grooves.

2.4 Evolution of Turbulence at $\phi = 0.28$

This section summarizes the evolution of turbulence in the passage and mechanisms affecting it. The data includes the turbulent kinetic energy (TKE) $k = 0.5(\langle u'_r u'_r \rangle + \langle u'_\theta u'_\theta \rangle + \langle u'_z u'_z \rangle)$, its components (i.e., the normal Reynolds stresses, $\langle u'_r u'_r \rangle$, $\langle u'_\theta u'_\theta \rangle$, and $\langle u'_z u'_z \rangle$) as well as the dominant contributors to turbulence production in the compressor. The TKE production rate is $P = 0.5(P_{rr} + P_{\theta\theta} + P_{zz})$, where

$$P_{rr} = -2 \left[\langle u'_r u'_z \rangle \frac{\partial U_r}{\partial z} + \langle u'_r{}^2 \rangle \frac{\partial U_r}{\partial r} - 2 \frac{\langle u'_r u'_\theta \rangle}{r} \frac{\partial U_r}{\partial \theta} + \langle u'_r u'_\theta \rangle \frac{\partial U_r}{r \partial \theta} \right]$$

$$P_{\theta\theta} = -2 \left[\langle u'_z u'_\theta \rangle \frac{\partial U_\theta}{\partial z} + \langle u'_r u'_\theta \rangle \frac{\partial U_\theta}{\partial r} + \frac{\langle u'_\theta{}^2 \rangle}{r} \left(\frac{\partial U_\theta}{\partial \theta} + U_r \right) + \frac{\langle u'_r u'_\theta \rangle}{r} U_\theta \right]$$

$$P_{zz} = -2 \left[\langle u'_z{}^2 \rangle \frac{\partial U_z}{\partial z} + \langle u'_r u'_z \rangle \frac{\partial U_z}{\partial r} + \langle u'_z u'_\theta \rangle \frac{\partial U_z}{r \partial \theta} \right]$$

are the production rates of the corresponding normal stress components (Ref. 25). The only terms that cannot be calculated from the present planar data are those involving $\partial U_\theta / \partial z$ and $\partial U_r / \partial z$. Terms containing $\partial U_z / \partial z$ can be obtained using the continuity equation. To obtain the missing terms one can either perform volumetric measurements (using, e.g., tomographic PIV, planned for the next round of measurements), or acquire data in a series of closely spaced planes, as we have done before in meridional planes in the tip region of the same machine (Refs. 8, 11, and 12). In the following figures, the stresses are normalized by U_T^2 , and the production terms by ΩU_T^2 , where Ω is the angular velocity of the machine (50.24 rad/s).

2.4.1 Turbulence in the Rotor Passage

Starting from the untreated endwall at $\phi = 0.28$, Figure 19 shows the distribution of TKE, $\langle u'_z u'_z \rangle$, and $\langle u'_\theta u'_\theta \rangle$ upstream of the rotor, corresponding to the flow structure depicted in Figure 5(a) to (c). The TKE (Figure 19(a)) is elevated in the IGV wakes and along the casing, especially near the PS of the blade tip. The dominant contributor is $\langle u'_z u'_z \rangle$ (Figure 19(b)), and its distribution appears to be similar to that of the TKE. The IGV wake has comparable contributions from $\langle u'_\theta u'_\theta \rangle$ (Figure 19(c)) and $\langle u'_z u'_z \rangle$, but the axial component is significantly larger along the tip, especially in the IGV-casing junction and in the PS of the rotor blade tip. The latter region is affected by the intermittent propagation of backflow vortices. The radial normal term, $\langle u'_r u'_r \rangle$ (not shown), is significantly lower than the other components in this plane.

Figure 20 shows the evolution of the TKE and the dominant Reynolds stress terms as the flow passes through the rotor. As a general observation, the axial velocity fluctuations are extremely high, with peak rms values of almost 70 percent of V_z (i.e., $(\langle u'_z u'_z \rangle)^{0.5} \sim 0.2U_T = 0.71V_z$), providing statistical evidence

for the extent of flow instability in the rotor passage. The instantaneous axial velocity (e.g., Figure 10 for $z/c_a = 0.28$) fluctuates in magnitude and area from reverse flow, reaching $-2V_z$ in almost 80 percent of the passage, to high axial velocity throughout the passage. Such large fluctuations would be a challenge to model. At $z/c_a = 0.28$, the TKE is high in the entire outer 30 percent of the span. It peaks in the tip gap and in the SS of the blade tip and remains high along a large fraction of the interface between regions of low U_z and high U_θ in the outer span, and the inner region with high U_z and moderate U_θ underneath it. Both $\langle u'_z u'_z \rangle$ and $\langle u'_\theta u'_\theta \rangle$ are significant contributors, but not in the same location and not to the same extent, demonstrating the inhomogeneity and anisotropy of the turbulence. In this plane, $\langle u'_\theta u'_\theta \rangle$ is the largest term, peaking near the SS of the blade tip and in the tip gap. It also has elevated values near the casing and along the interface of tip flow and passage flow. There is a peak in $\langle u'_z u'_z \rangle$ in the tip gap, and its magnitude is also high along the interface. The magnitude of $\langle u'_r u'_r \rangle$ (not shown) is not negligible, but it is significantly smaller than the other components.

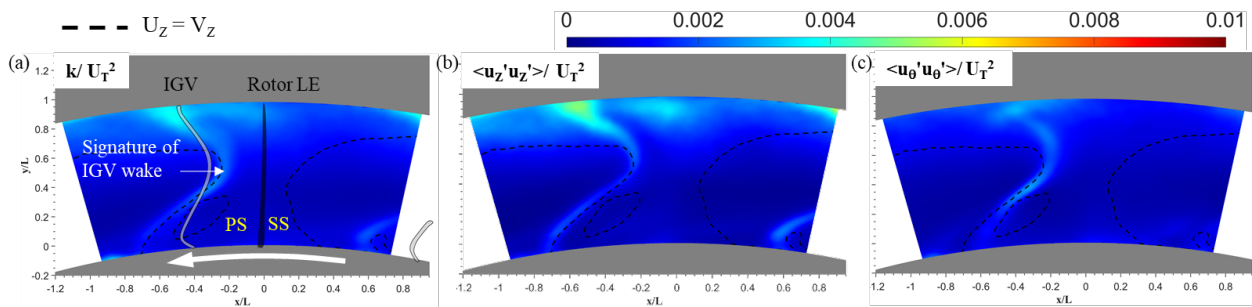


Figure 19.—Distribution of (a) TKE, (b) $\langle u'_z u'_z \rangle$, and (c) $\langle u'_\theta u'_\theta \rangle$ upstream of the rotor at $\varphi = 0.28$. The location of the rotor LE is shown ($\Theta = 0$) in (a).

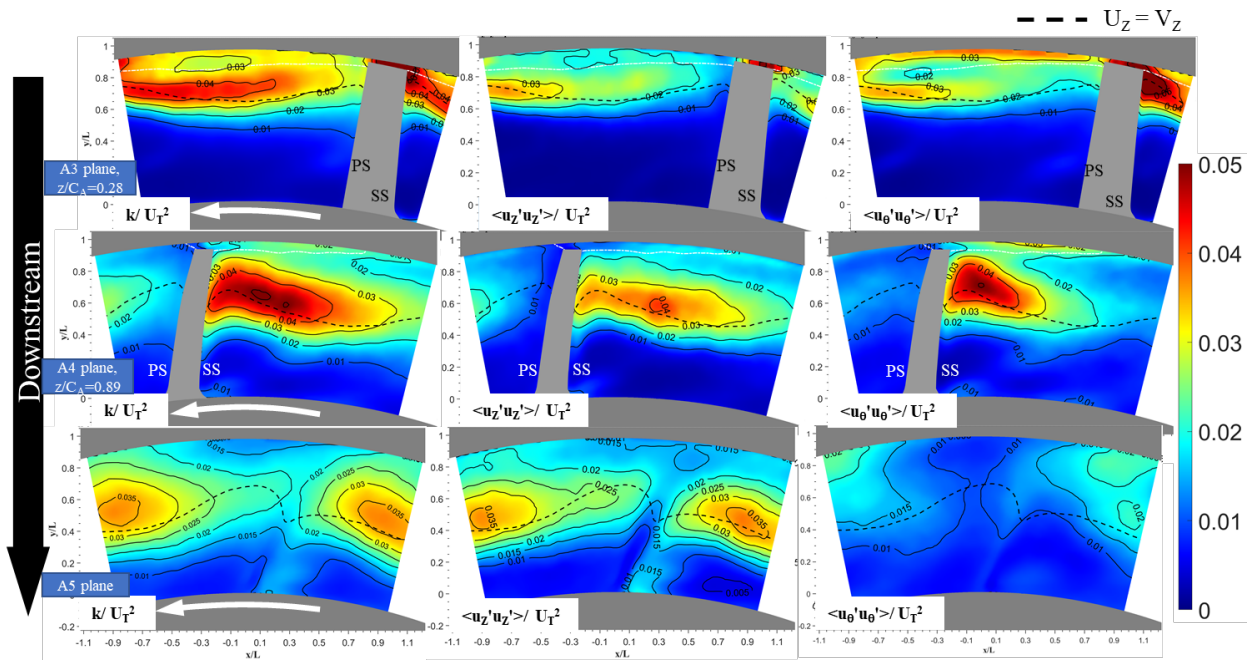


Figure 20.—Distribution of TKE and dominant normal Reynolds stresses at (top row) $z/c_a = 0.28$, (middle row) $z/c_a = 0.89$, and (bottom row) downstream of the rotor at $\varphi = 0.28$. The corresponding mean flow is presented in Figure 8.

Further towards the TE, at $z/c_a = 0.89$, the TKE is maximum along the interface between high- and low-momentum regions, which is now located deeper in the passage, peaking close to the blade SS. The turbulence is still elevated over the outer 50 percent of the passage but does not have a maximum near the blade tip. This trend should be expected since most of the TLV and BFVs roll up, and interactions occur further upstream. Whereas the distribution of $\langle u'_z u'_z \rangle$ remains broad and even higher in magnitude than its value further upstream, the magnitude of $\langle u'_\theta u'_\theta \rangle$ decreases and remains concentrated near the SS of the blade. Downstream of the rotor, the TKE is still high but is significantly lower than that in the passage, still peaking along the interface between the low- U_z , high- U_θ region in the outer part and the high- U_z , moderate- U_θ area in the inner part of the passage. The decrease in TKE is predominantly associated with a considerable reduction in the magnitude of $\langle u'_\theta u'_\theta \rangle$, while $\langle u'_z u'_z \rangle$ remains high, with only a slight decline. Clearly, each normal Reynolds stress component evolves in a different manner, in addition to the differences in their magnitude and spatial distributions. Some of the mechanisms affecting these trends are discussed below. Figure 21 demonstrates the changes to the TKE distribution with blade orientation downstream of the rotor. As is evident, the entire pattern rotates with the blade wake, always peaking on the SS of the wake.

The effects of the ACGs on the distribution of TKE before and after the rotor are demonstrated in Figure 22. Upstream of the rotor, the turbulence is high along the shear layer formed as the flow jetting out from the grooves meets the passage flow. Here, $\langle u'_z u'_z \rangle$ (not shown) is the dominant component along the entire shear layer, and $\langle u'_\theta u'_\theta \rangle$ (not shown) is elevated within the vortex but has a lower magnitude than the axial term. The flow is stabilized by ingestion of the TLV, reduction of the axial momentum deficit and the area with high U_θ , and elimination of the BFVs by the ACGs, which results in a substantial decrease in the turbulence level downstream of the rotor. The TKE remains elevated in the rotor wake and in the area with radial gradients in U_θ on the pressure side of the wake, but it is nowhere close in magnitude to that of the rotor casing with untreated endwall.

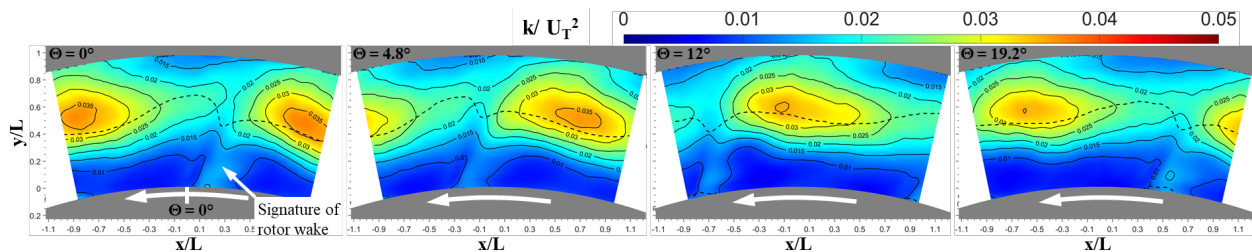


Figure 21.—Variations in TKE distribution downstream of the rotor with blade orientation (indicated on each plot) for a smooth endwall at $\phi = 0.28$.

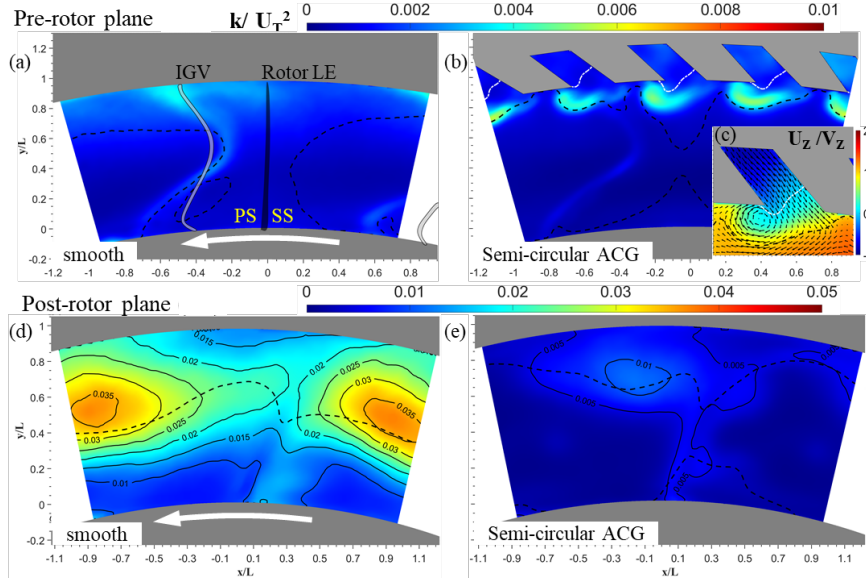


Figure 22.—The effect of axial casing grooves on the TKE distributions upstream and downstream of the rotor at $\varphi = 0.28$ for (left column, a,c) untreated endwall and (right column, b,d) with semicircular ACGs installed. (Top row, a,b,c) upstream of the rotor and (bottom row, d,e) downstream of the rotor. (c) Zoomed-in section showing the axial velocity contours near the exit from the ACG overlaid on the in-plane velocity vectors.

2.4.2 Production Rate of Turbulence in the Rotor Passage

Some, but not all, of the observed changes to the turbulence in the passage can be explained by examining the dominant production rate terms. To obtain a complete picture, one must also account for the distributions of advection by mean flow, transport by turbulence, correlations between pressure and rate of strain, and dissipation rate. It was already shown that in the tip region, all of the terms in the Reynolds stress transport equations should be accounted for (Refs. 11 and 12). However, this report focuses on contributions to the production rate; that is, sources of turbulence resulting from interactions of the Reynolds stresses with the mean strain rate field. Upstream of the rotor, $-2\langle u_z'^2 \rangle \partial U_z / \partial z$ (not shown), the axial contraction associated with blockage at the beginning of the rotor, is the dominant contributor to the production of $\langle u_z' u_z' \rangle$. The dominant contributors to the increase in $\langle u_\theta' u_\theta' \rangle$ at the beginning of the rotor passage ($z/c_a = 0.28$, Figure 20(a)) are presented in Figure 22. Here, shear production, namely $-2\langle u_r' u_\theta' \rangle \partial U_\theta / \partial r$, and circumferential contraction, $-2\langle u_\theta'^2 \rangle (\partial U_\theta / r \partial \theta)$, have comparable magnitude and play significant roles. The circumferential contraction term peaks near the SS of the blade tip and is negative in the region of circumferential extension near the PS of the blade. As expected, the shear production peaks along the interface between the outer and inner flow regions because of the high values of $\partial U_\theta / \partial r$ there. The correspondence between these production terms and the distribution of $\langle u_\theta' u_\theta' \rangle$ is evident.

At $z/c_a = 0.89$, none of the production rate terms that could be calculated from the present data explains the distribution of high $\langle u_\theta' u_\theta' \rangle$. As for the missing shear production term, $-2\langle u_z' u_\theta' \rangle \partial U_\theta / \partial z$, the distribution of $\langle u_z' u_\theta' \rangle$ (not shown, see Ref. 3) shows a peak near the SS of the blade in the same region as the $\langle u_\theta' u_\theta' \rangle$ peak (Figure 20(b)). Also, the sign of $\partial U_\theta / \partial z$ is expected to be positive since U_θ increases axially near the blade SS (compare Figure 8(b) to (e)). Hence, it is likely that this term causes the $\langle u_\theta' u_\theta' \rangle$ peak in the blade SS in the aft part of the rotor passage.

As for the production rate of $\langle u'_z u'_z \rangle$, Figure 24 shows the evolution of the dominant contributor, $-2\langle u'_r u'_z \rangle \partial U_z / \partial r$, in the rotor passage. Whereas this term peaks at the interface between the tip flow and the passage flow, consistent with the distribution of $\langle u'_z u'_z \rangle$, its magnitude decays axially, in contrast to the near-constant level of the axial normal stress. Hence, in this case, streamwise advection of turbulence from upstream planes must play a significant role. A more complete analysis of the terms in the Reynolds stress transport equations, which are planned for the near future, will investigate this.

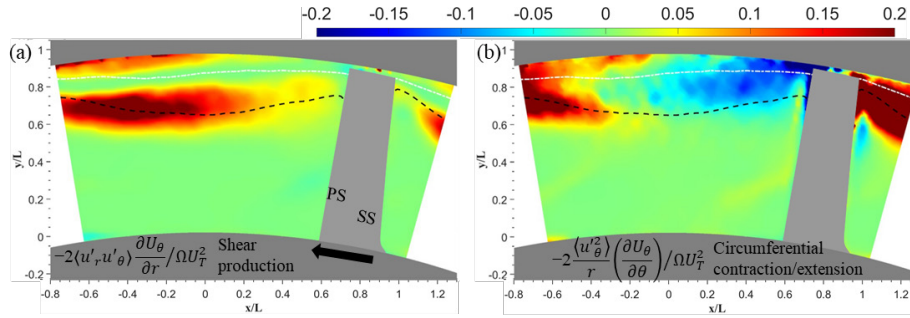


Figure 23.—Distribution of dominant production rate terms of $\langle u'_\theta u'_\theta \rangle$ at $z/c_a = 0.28$ for $\phi = 0.28$ and a smooth endwall: (a) $-2\langle u'_r u'_\theta \rangle \frac{\partial U_\theta}{\partial r} / \Omega U_T^2$ and (b) $-2\langle u'_\theta \rangle \frac{1}{r} \left(\frac{\partial U_\theta}{\partial \theta} \right) / \Omega U_T^2$.

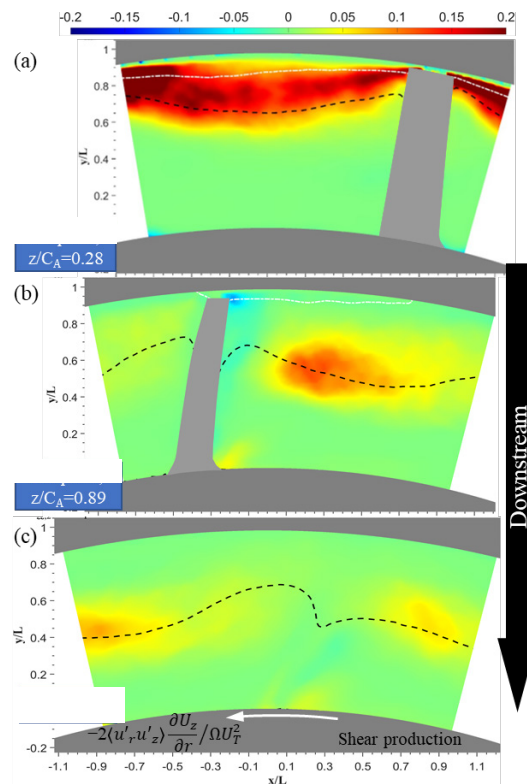


Figure 24.—Distributions of $-2\langle u'_r u'_z \rangle \frac{\partial U_z}{\partial r} / \Omega U_T^2$, the dominant contributor to $\langle u'_z u'_z \rangle$ production in the rotor passage at $\phi = 0.28$, for smooth endwall. (a) $z/c_a = 0.28$, (b) $z/c_a = 0.89$, and (c) downstream of the rotor.

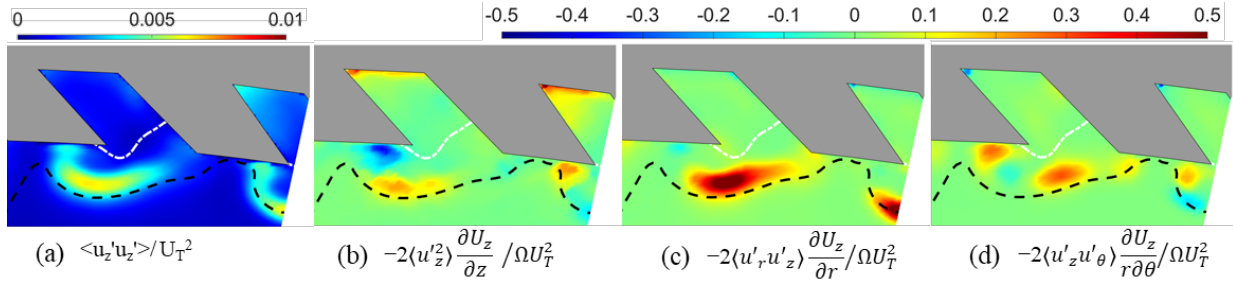


Figure 25.—Distribution of $\langle u'_z u'_z \rangle$ and its production rate terms near exit from the semi-circular axial casing grooves upstream of the rotor at $\phi = 0.28$.

Finally, the contributors to production of $\langle u'_z u'_z \rangle$ at the exit from the casing grooves are compared to the distribution of this stress in Figure 25. Here, $-2\langle u'_r u'_z \rangle \partial U_z / \partial r$ is the dominant term owing to the high magnitude of $\partial U_z / \partial r$ in the shear layer generated between the outflow from the groove outflow and the passage flow. The other terms also have peaks along this interface, but their magnitudes are lower.

2.4.3 Evolution of Turbulence In and Downstream of Stator at $\phi = 0.28$

Figure 26 follows the evolution of TKE and normal Reynolds stresses as the flow passes through the stator. The first row shows the results for the rotor-stator gap, the same data as in Figure 20(c), but at a different scale. All the contours are plotted using the same color scales to demonstrate the rapid decay in TKE and normal stresses that occur in the stator. Although the turbulence is still high over the entire outer part of the rotor-stator gap, as previously discussed, as the flow reaches the $z/c_a = 0.10$ plane, the TKE decreases by more than 50 percent in most of the tip region except for the vicinity of the stator blade SS. Upon reaching the $z/c_a = 0.71$ plane, all remnants of high TKE in the outer part of the passage are dissipated. The only place with elevated TKE is located along the lower half of the SS of the blade, in the area where the boundary layer becomes unstable. Downstream of the stator, the TKE level is even lower, and regions with slightly elevated TKE are confined to the lower half of the passage in the region that coincides with the stator wake and the elevated turbulence in the SS boundary layer.

The distributions of normal Reynolds stresses display both anisotropy and spatial inhomogeneity at all PIV planes, with components following different trends and peaking at different locations. For example, at $z/c_a = 0.10$, $\langle u'_z u'_z \rangle$ decays rapidly, $\langle u'_r u'_r \rangle$ remains at a similar level to that observed upstream of the stator, and $\langle u'_\theta u'_\theta \rangle$ decays in most areas except for the casing and the outer SS of the blade, where it becomes the main contributor to the high TKE. By $z/c_a = 0.71$, $\langle u'_r u'_r \rangle$ and $\langle u'_\theta u'_\theta \rangle$ have decayed considerably, but $\langle u'_z u'_z \rangle$ increases along the lower part of the SS boundary layer. All components decrease at the exit from the stator, with $\langle u'_r u'_r \rangle$ becoming very small, $\langle u'_\theta u'_\theta \rangle$ remaining slightly elevated in the blade wake, and $\langle u'_z u'_z \rangle$ remaining high in the SS of the wake, becoming the main contributor to the TKE.

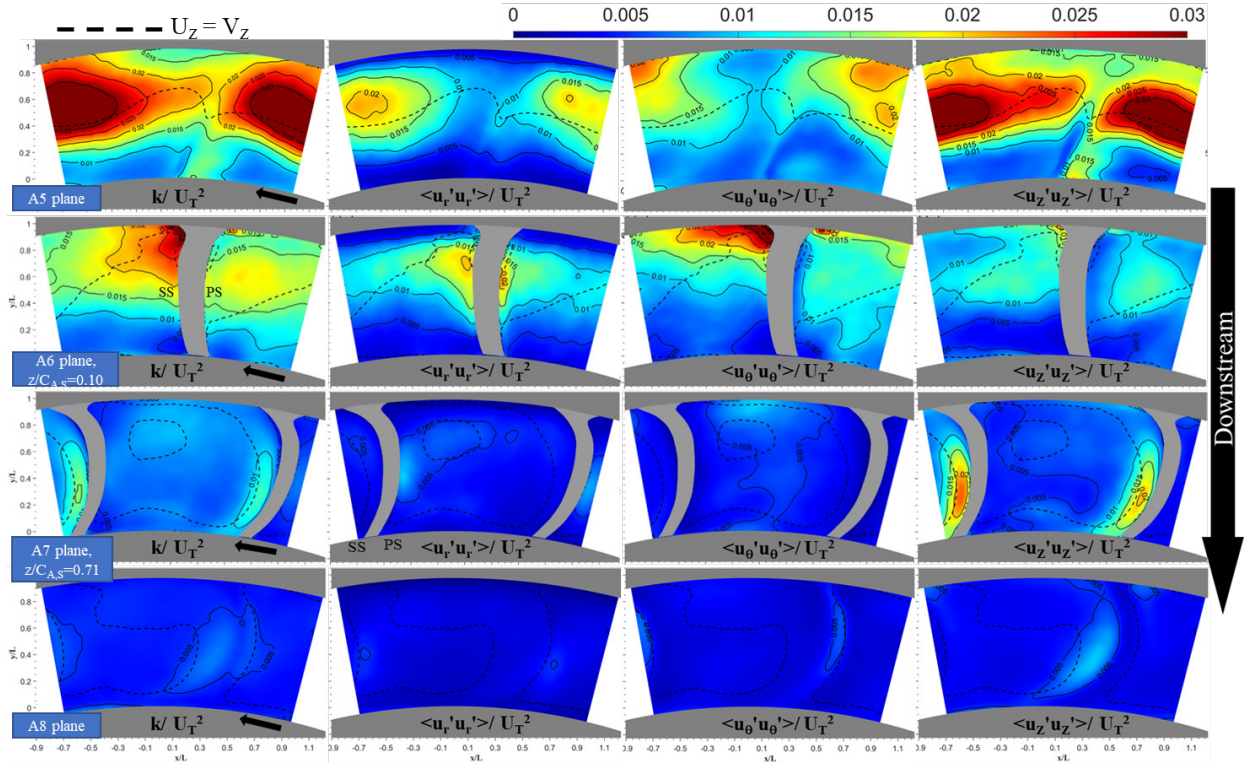


Figure 26.—Evolution of TKE k/U_T^2 and normal Reynolds stresses in the stator passage at $\phi = 0.28$. Top row: at exit from rotor, second row: at $z/c_a = 0.10$, third row: at $z/c_a = 0.71$, and bottom row: downstream of the stator. Dashed lines: $U_z/V_z = 1$.

To elucidate some of the observed trends of the normal Reynolds stresses, Figure 27 shows selected distributions of dominant production rate terms. At $z/c_a = 0.1$, the high $\langle u'_\theta u'_\theta \rangle$ near the casing and SS of the blade could not be explained from the available production terms. However, one of the missing terms, $-2\langle u'_z u'_\theta \rangle \partial U_\theta / \partial z$, is expected to be positive there, based on the negative values of $-\langle u'_z u'_\theta \rangle$ (not shown) and the negative sign of $\partial U_\theta / \partial z$ evaluated from the decrease in U_θ (Figure 20) in the region of high $\langle u'_\theta u'_\theta \rangle$. Because of the axial stretching of the flow, $\partial U_z / \partial z > 0$, and $-2\langle u_z'^2 \rangle \frac{\partial U_z}{\partial z} / \Omega U_T^2$ over a broad area except for the tip corner (Figure 27(a)); hence, $\langle u'_z u'_z \rangle$ decays almost everywhere except for the SS tip corner. At $z/c_a = 0.71$, $-2\langle u_z'^2 \rangle \partial U_z / \partial z > 0$ and $-2\langle u'_z u'_\theta \rangle \partial U_z / \partial \theta < 0$ in the lower SS of the blade boundary layer (Figure 27(b) and (c)), in the region of high $\langle u'_z u'_z \rangle$. Since the magnitude of axial contraction is much higher than that of the shear production term, the observed trends are expected. As mentioned before, this region experiences intermittent boundary layer separation, a likely outcome of the adverse axial pressure gradients $U_z \partial U_z / \partial z < 0$ there. At the trailing edge and downstream of the stator, while all the components decay, the axial contraction persists, resulting in a slower decay of $\langle u'_z u'_z \rangle$.

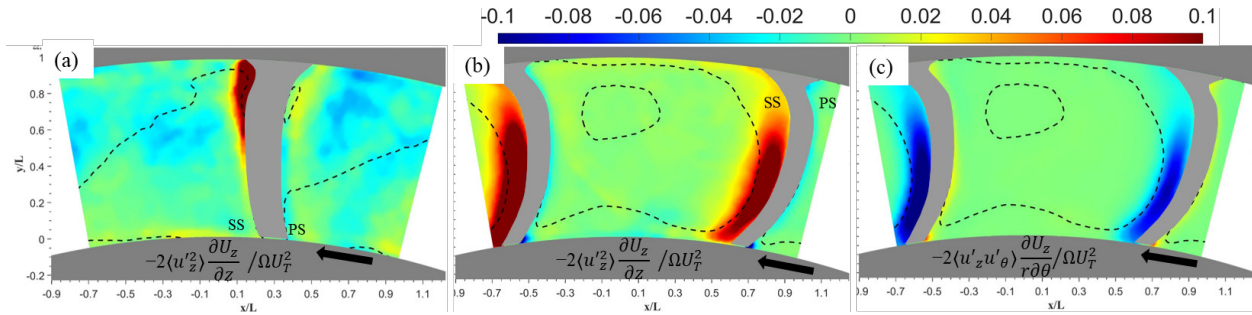


Figure 27.—Distribution of selected dominant terms affecting production rate of turbulence in stator passage at $\varphi = 0.28$ and smooth endwall. (a) $-2\langle u_z'^2 \rangle \frac{\partial U_z}{\partial z} / \Omega U_T^2$ at $z/c_a = 0.1$. (b) $-2\langle u_z'^2 \rangle \frac{\partial U_z}{\partial z} / \Omega U_T^2$ at $z/c_a = 0.71$, and (c) $-2\langle u_z'u'_\theta \rangle \frac{\partial U_z}{r\partial\theta} / \Omega U_T^2$ at $z/c_a = 0.71$.

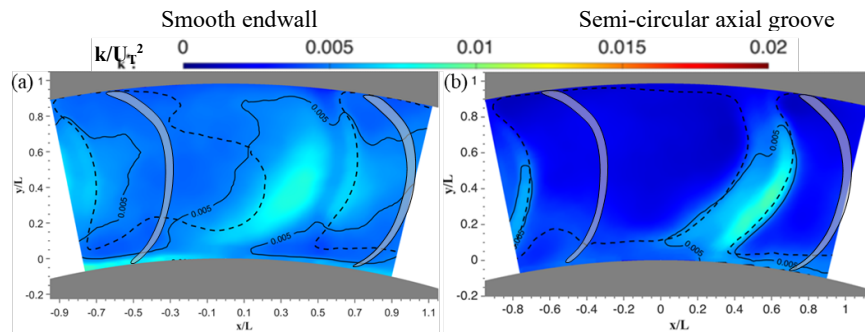


Figure 28.—Distribution of turbulent kinetic energy normalized by U_T^2 downstream of the stator at $\varphi = 0.28$: (a) smooth endwall and (b) semi-circular ACG.

Finally, Figure 28 is a comparison of the TKE distributions downstream of the stator for a smooth endwall to distributions measured for the stator with semicircular ACGs. As is evident, the grooves cause a reduction in TKE almost everywhere except for the now much narrower stator wake (compare Figure 12 and Figure 13).

2.5 Evolution of Turbulence at $\varphi = 0.37$ (Near BEP)

This section discusses the evolution of turbulence for pre-stall flow rate $\varphi = 0.37$; that is, at the best efficiency point for the untreated endwall. Figure 29 compares the TKE across the entire machine for an untreated endwall (on the left column) to that measured with the semicircular ACGs installed (on the right column). Upstream of the rotor, the turbulence level for the smooth endwall is considerably lower than that at the pre-stall flow rate (see Figure 22(a)), with the IGV wake being the only place with elevated turbulence. With the ACGs installed, the TKE is high along the shear layer at the interface between the outflow from the groove flow and the passage flow. The magnitudes and the widths of elevated turbulence regions are smaller than those occurring at pre-stall (Figure 22(b)), but the mechanisms involved are similar.

Downstream of the rotor (Figure 29(b)) and at $\phi = 0.37$, the mean flow structures with and without casing grooves are quite similar (Figure 15 and Figure 16). Hence, it is not surprising that the distributions of TKE are similar. However, the peak for the untreated endwall appears to be more concentrated, and that of the ACG is more broadly distributed with a lower peak value. Their magnitudes are significantly lower than that observed for the untreated endwall at pre-stall conditions (Figure 22(b), column I), providing statistical evidence for the flow stability at $\phi = 0.37$. In contrast, the magnitude and distribution of TKE are not very different from those at pre-stall condition with the ACGs installed (Figure 22(b), row II; note the different scales). In both cases, the TKE downstream of the rotor at $\phi = 0.37$ is elevated along the casing where the axial momentum is low, peaking near the TLV (see Figure 15 and Figure 16), as well as in the rotor wake, and in secondary hub structures. Interestingly, there is also a mild but distinct peak corresponding to the IGV wake in the middle of the passage (compare with Figure 15(c), column III), demonstrating that when the flow is stable, the IGV impact on the turbulence persists across the rotor. Finally, downstream of the stator, the flow structure and distribution of TKE for untreated endwall and ACG (Figure 29(c)) are very similar. The TKE is elevated along the stator wake, in the outer span of the passage, and in the secondary hub structures observed at the PS of the stator blade wake.

Although the data are available, this report does not provide a complete breakdown of the evolution of all the normal Reynolds stress terms at the BEP. Instead, the focus is on the distribution of $\langle u'_z u'_z \rangle$, the dominant contributor to the TKE at the exit from the rotor. Figure 30 compares the distributions of $\langle u'_z u'_z \rangle$ for a smooth endwall to that with the ACGs installed. Similar to the trends of the TKE, the peak of $\langle u'_z u'_z \rangle$ for a smooth endwall is higher and is concentrated in a small area, whereas the peak with ACG has a smaller magnitude but is distributed over a broader area. An explanation for the difference between them can be found in prior meridional plane measurements focusing on the tip region. As discussed and demonstrated in Chen et al. (Ref. 7), broadening of the TKE peak at the BEP flow rate is caused by interaction of the TLV with the flow in the groove. Figure 31 presents meridional plane distributions of circumferential vorticity and TKE downstream of the groove. At the BEP flow rate, there is intermittent in- and out-flow from the downstream end of the groove. The inflow occurs when the blade PS is exposed to the downstream end of the groove. In contrast, when the downstream end is exposed to the blade SS, the TLV entrains secondary flow structures from the groove into the passage. The sample distribution in Figure 31 demonstrates the latter phase; that is, when the TLV entrains secondary vortices from the groove into the passage. Consequently, the TLV becomes fragmented with multiple vortices distributed over a large area, which upon ensemble averaging, appear as a broad area with distributed vorticity and elevated TKE. In contrast, for a smooth endwall, the multiple vortical structures comprising the TLV center remain concentrated in a relatively small area, which has higher peak turbulence level. Eventually, this vortex breaks down as well, presumably under the influence of backflow vortices (Ref. 8).

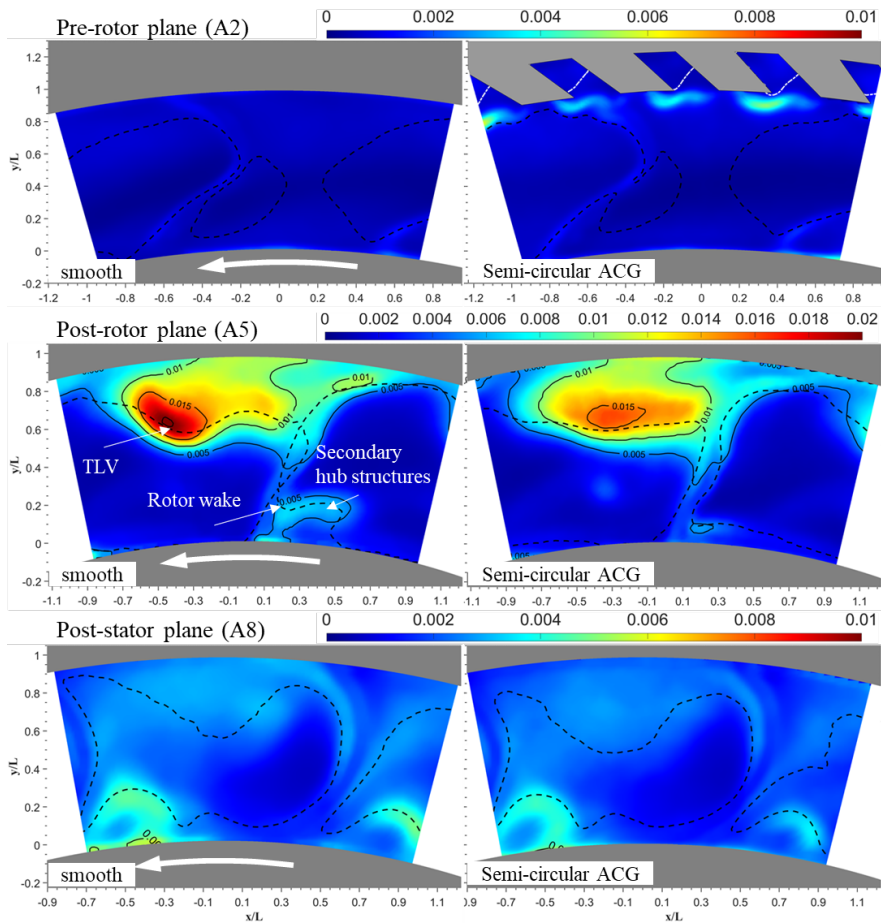


Figure 29.—Comparison of the evolution of TKE across the entire machine between (left) smooth endwall and (right) semicircular ACG at $\phi = 0.37$. Dashed lines: $U_z/V_z = 1$.

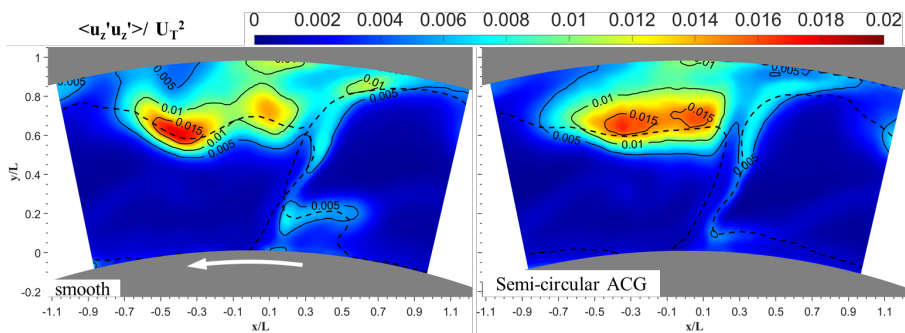


Figure 30.—Distribution of $\langle u'_z u'_z \rangle / U_T^2$ for (left) Smooth endwall and (right) semicircular ACG downstream of the rotor at $\phi = 0.37$.

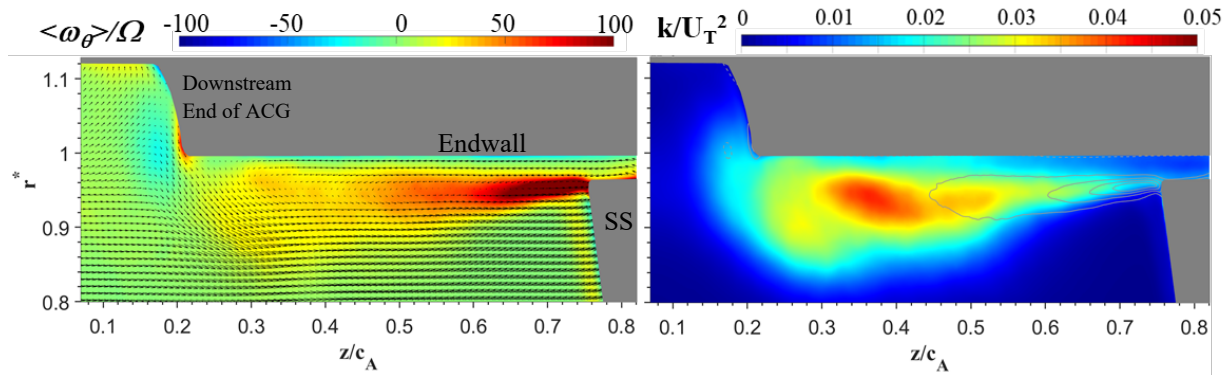


Figure 31.—Distributions of (left) circumferential vorticity (color contours) overlaid on the in-plane velocity vectors and (right) TKE in a meridional plane focusing on the tip region downstream of the semicircular ACG at $\varphi = 0.38$ (Ref. 7). Here, $r^* = (r - r_{\text{hub}})/r_{\text{tip}} - r_{\text{hub}}$.

3.0 Concluding Remarks

Analysis of the data acquired under this project is still in progress, and additional information can be found in the two papers recently submitted to 2022 Turbo Expo. Another publication, which is presently under preparation, will focus on the structure of the turbulence; in particular, the properties of the anisotropy tensor as well as the transport of turbulence in the passage. As part of the ongoing analysis, we examine the relationships between the Reynolds stress and the mean strain rate tensors. The measured eddy viscosity can be calculated from the ratio between corresponding stress and strain components. Results show that owing to the extreme non-equilibrium conditions within the machine, as well as the anisotropy and inhomogeneity of the turbulence, the spatial distribution of eddy viscosity varies by orders of magnitude and even in sign among the stress/strain components. Yet, a recent analysis of tip flow data from several turbomachines (Refs. 11 and 12) has revealed that certain features of the eddy viscosity tend to repeat themselves for the same stress component, in spite of substantial differences in load distributions and operating conditions. These findings raise the possibility that machine-learning-based modeling tools could be developed for turbomachinery flows. The present measurements also demonstrate that analysis accounts for the complexity of the flow in turbomachines by following the evolution of production, transport, and dissipation of turbulence (i.e., by solving the full Reynolds stress transport equations), is more likely to succeed than models assuming local equilibrium. The type of data that the present project has generated is fundamental to any future attempts to develop more appropriate Reynolds stress models.

References

1. Saraswat, Ayush; Koley, Subhra Shankha; and Katz, Joseph: Experimental Characterization of the Evolution of Global Flow Structure in the Passage of an Axial Compressor. ASME GT2021-60325, 2021.
2. Saraswat, A.; Koley, S.S.; and Katz, J.: Impact of Operating Conditions and Axial Casing Grooves on the Evolution of Flow Structure Across Blade Rows in an Axial Compressor. ASME Turbo Expo, Rotterdam, The Netherlands, 2022.
3. Koley, S.S.; Saraswat, A.; and Katz, J.: Evolution of Turbulence and Its Modification by Axial Casing Grooves in a Multi-Stage Axial Compressor. ASME Turbo Expo., Rotterdam, The Netherlands, 2022.

4. Koley, Subhra Shankha, et al.: Effect of Axial Casing Groove Geometry on the Rotor-Groove Interactions in the Tip Region of a Compressor. *J. Turbomach.*, vol. 143, no. 9, 2021, pp. 091010–1—091010–17.
5. Chen, Huang, et al.: Effects of Axial Casing Grooves on the Structure of Turbulence in the Tip Region of an Axial Turbomachine Rotor. *J. Turbomach.*, vol. 143, no. 9, 2021, pp. 091009–1—091009–14.
6. Koley, Subhra Shankha, et al.: Effect of the Axial Casing Groove Geometry on the Production and Distribution of Reynolds Stresses in the Tip Region of an Axial Compressor Rotor. *J. Turbomach.* vol. 144, no. 9, 2021, pp. 091007–1—091007–12.
7. Chen, Huang; Li, Yuanchao; and Katz, Joseph: On the Interactions of a Rotor Blade Tip Flow With Axial Casing Grooves in an Axial Compressor Near the Best Efficiency Point. *J. Turbomach.*, vol. 141, no. 1, 2019, pp. 011008–1—011008–14.
8. Chen, Huang, et al.: Visualizations of Flow Structures in the Rotor Passage of an Axial Compressor at the Onset of Stall. *J. Turbomach.*, vol. 139, no. 4, 2017, pp. 041008–1—041008–14.
9. Chen, Huang, et al.: Systematic Experimental Evaluations Aimed at Optimizing the Geometry of Axial Casing Groove in a Compressor. *ASME GT2019–91050*, 2019.
10. Chen, Huang, et al.: Effects of Axial Casing Grooves on the Structure of Turbulence in the Tip Region of an Axial Turbomachine Rotor. *J. Turbomach.*, vol. 143, no. 9, 2021, pp. 091009–1—091009–14.
11. Li, Yuanchao; Chen, Huang; and Katz, Joseph: Measurements and Characterization of Turbulence in the Tip Region of an Axial Compressor Rotor. *J. Turbomach.*, vol. 139, no. 12, 2017, pp. 121003–1—121003–10.
12. Li, Yuanchao; Chen, Huang; and Katz, Joseph: Challenges in Modeling of Turbulence in the Tip Region of Axial Turbomachines. *J. Sh. Res.*, vol. 63, no. 1, 2019, pp. 56–68.
13. Li, Yuanchao, et al.: On the Effects of Tip Clearance and Operating Condition on the Flow Structures Within an Axial Turbomachine Rotor Passage. *J. Turbomach.*, vol. 141, no. 11, 2019, pp. 111002–1—111002–13.
14. Tan, David, et al.: Visualization and Time-Resolved Particle Image Velocimetry Measurements of the Flow in the Tip Region of a Subsonic Compressor Rotor. *J. Turbomach.*, vol. 137, no. 4, 2015, pp. 041007–1—041007–11.
15. Tan, D., et al.: Effect of Large Scale Cavitating Vortical Structures on Performance Breakdown in Axial Waterjet Pumps. *J. Fluids Eng.*, vol. 137, no. 11, 2015, p. 111301.
16. Chen, Huang, et al.: Experimental Investigations of Cavitation Performance Breakdown in an Axial Waterjet Pump. *J. Fluids Eng.*, vol. 142, no. 9, 2020, pp. 191204–1—191204–15.
17. Wu, Huixuan; Miorini, Rinaldo L.; and Katz, Joseph: Measurements of the Tip Leakage Vortex Structures and Turbulence in the Meridional Plane of an Axial Water-Jet Pump. *Exp. Fluids*, vol. 50, no. 4, 2011, pp. 989–1003.
18. Wu, Huixuan, et al.: Turbulence Within the Tip-Leakage Vortex of an Axial Waterjet Pump. *AIAA J.*, vol. 50, no. 11, 2012, pp. 2574–2587.
19. Wu, Huixuan, et al.: Three-Dimensional Flow Structures and Associated Turbulence in the Tip Region of a Waterjet Pump Rotor Blade. *Exp. Fluids*, vol. 51, no. 6, 2011, pp. 1721–1737.
20. Miorini, Rinaldo L.; Wu, Huixuan; and Katz, Joseph: The Internal Structure of the Tip Leakage Vortex Within the Rotor of an Axial Waterjet Pump. *J. Turbomach.*, vol. 134, no. 3, 2011, pp. 031018–1—031018-12.

21. Chen, Huang, et al.: An Experimental Study of Stall Suppression and Associated Changes to the Flow Structures in the Tip Region of an Axial Low Speed Fan Rotor by Axial Casing Grooves. *J. Turbomach.*, vol. 139, no. 12, 2017, pp. 121010-1—121010-14.
22. Hah, Chunill; Hathaway, Michael; and Katz, J.: Investigation of Unsteady Flow Field in a Low-Speed One and a Half Stage Axial Compressor: Effects of Tip Gap Size on the Tip Clearance Flow Structure at Near Stall Operation. *ASME GT2014-27094*, 2014.
23. Tan, David, et al.: Visualization and Time-Resolved Particle Image Velocimetry Measurements of the Flow in the Tip Region of a Subsonic Compressor Rotor. *J. Turbomach.*, vol. 137, no. 4, 2014, pp. 041007-1—041007-11.
24. Muller, M.W., et al.: Investigation of Passage Flow Features in a Transonic Compressor Rotor With Casing Treatments. *ASME GT2011-45364*, 2011.
25. Lakshminarayana, B.: Turbulence Modeling for Complex Shear Flows. *AIAA J.*, vol. 24, no. 12, 1986, pp. 1900-1917.

